University of Zurich[UZH]

Development of Analysis Methods for Detecting Color Centers in Crystals

Master Thesis

Valentino Aerne

Supervised by

Prof. Dr. Laura Baudis & Gabriela R. Araujo

Abstract

The role of low-energy threshold detectors has become increasingly important for a range of novel applications. One of these applications is the search for dark matter, a type of matter that does not interact via electromagnetic force and constitutes a large portion of the total mass in our universe. Low-energy threshold detectors are particularly sensitive to Weakly Interacting Massive Particles (WIMPs) in the 0.3 - 3 GeV mass range. Moreover, they play a crucial role in the realm of neutrinos, providing a pathway to detect and analyze Coherent Elastic Neutrino-Nucleus Scattering (CEνNS) events. Although theoretically predicted over 40 years ago, nuclear recoils from such interactions have only recently been observed. Despite this groundbreaking discovery, the detection of CEνNS with neutrinos originating from reactors has not yet been achieved. This is due to the lower energy of reactor-produced neutrinos, which makes them harder to detect.

A promising development in this field is the PALEOCCENE (PAssive Low Energy Optical Color CEnter Nuclear rEcoil) concept, introducing a novel method for detecting low-energy nuclear recoils. Unlike current detectors that often require specific conditions such as high voltage or cryogenic temperatures, PALEOCCENE detectors can operate passively at room temperature, thus being versatile for various applications.

The basic mechanism of PALEOCCENE is based on the displacement of atoms in a crystal lattice when a nucleus undergoes recoil. If the energy from this recoil is high enough, a permanent vacancy can form. Such vacancies can lead to color centers that can absorb and re-emit light. We aim to detect these color centers by using Selective Plane Illumination Microscopy (SPIM). SPIM is a fluorescence microscopy technique that illuminates a specimen with a thin sheet of light, usually coming from the side, rather than simultaneously illuminating the entire sample volume at once. By moving the light sheet and the detection plane through the sample, three-dimensional imaging is obtained.

The datasets produced in SPIM scans are large, with sizes up to 23 GB and approximately 12 billion pixels. It is important to note, however, that these datasets only capture a portion of the crystal. In order to identify the signals from rare events from CEνNS and WIMP-nucleus scatterings the data has to be analyzed

not only in detail but also efficiently. As a result, we need automated tools that can help in detecting and verifying the observations of color centers.

This thesis will cover the implementation of the analysis and processing methods for the microscopy data. As a first R&D step, we use SPIM data from gamma irradiated cubic (10 mm^3) CaF_2 crystals. One of the primary tasks is the definition of a region of interest for the datasets, which ensures that any distortions or artifacts introduced by the microscopy process are removed or minimized. This provides a cleaner and more accurate dataset for further analysis. The next task is to identify color center features within the dataset, attributed to radiation-induced damage in the crystals. In this context, our analysis studies color centers encompassing both single and multiple pixels, aiming to advance our understanding of color center formation and imaging.

These methods, developed on data from γ-irradiated crystals, were applied to the data taken from a neutron irradiated CaF_2 sample (cubic 10 mm^3), where the color center formation is similar to the production mechanism that is expected from CEνNS and WIMP-nucleus scattering events. We examined the number of high-intensity pixels, which consistently appear in the same location across multiple scans, to observe the effects of the irradiation. A significant excess was identified, surpassing the estimated number of random occurrences. This indicates that nuclear recoil-induced damages in the crystal are observable by using SPIM. These results represent a significant advancement in bringing the PALEOCCENE concept closer to a practical application in low-energy nuclear recoil detection.

Contents

1 Dark Matter

In the vast and complex Universe, one of the most mysterious puzzles that remain unsolved is Dark Matter (DM). Eluding direct detection, yet leaving its gravitational mark on the cosmos, Dark Matter forms the invisible cosmic framework around which galaxies revolve. This invisible matter, contributing approximately 85% [1] to all the matter in the Universe, drives the formation of structures in the cosmos, bending light across the Universe, and holding galaxies together. In this chapter, we will explore the evidence pointing to its existence, investigate a handful of the potential candidates, and highlight different experiments.

1.1 Evidence

The name DM was first introduced by Fritz Zwicky, a Swiss astronomer and physicist, in his influential paper on the mass-to-light ratio and the absence of visible mass in the Coma cluster. He emphasized the idea that the Universe must contain more mass than what was expected [2]. In addition to this observation, there are more evidences, which support the existence of DM. These observations range from the measurement of rotational velocities of galaxies over gravitational lensing to the explanation of thermal fluctuations of the cosmic microwave background (CMB).

Rubin and Ford in 1970 measured the rotational velocities of the Andromeda Galaxy [3]. The gravitational law and combined with the requirement for a circular motion implies that the velocity should decrease with increasing distance to the center of the galaxy, considering that the mass is located in the center

$$v(r) = \sqrt{\frac{GM(r)}{r}}. \tag{1}$$

However, they found a nearly constant velocity with increasing distance (Fig. 1). The mass contribution from the visible mass in the disk and the gas can not allow for such high velocities. Therefore, an additional mass contribution is needed, which could come from a DM halo.

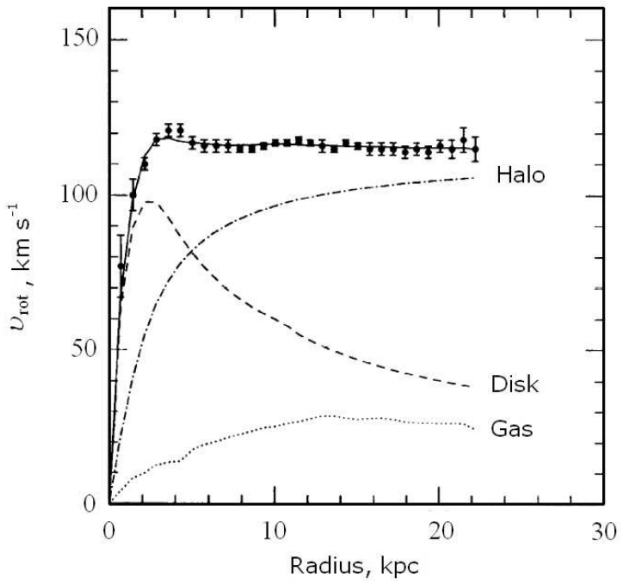

Figure 1: Rotational velocity of the galaxy NGC6503 [4]. Disk and Gas are the observed baryonic mass distributions. Halo represents the estimated DM contribution to match the observed rotational velocity.

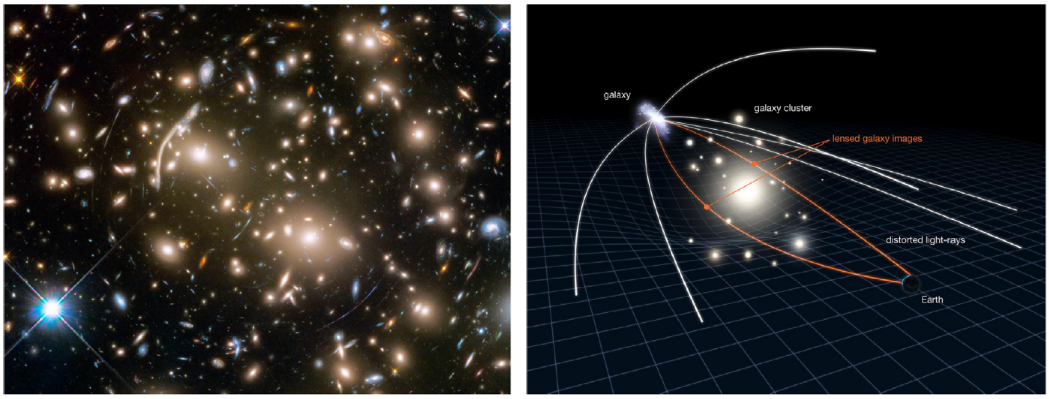

Figure 2: On the left, hundreds of galaxies in the galaxy cluster Abell 370. Images from galaxies are distorted and form arcs. On the right is the schematic explanation of the strong gravitational lensing [5].

One of the most striking indications of the presence of non-visible mass is the phenomenon of gravitational lensing, which occurs when the trajectory of photons is bent around massive objects (Fig. 2). This lensing effect is used to provide compelling evidence for the existence of dark matter. In the case of the bullet cluster, where two galaxy clusters collided head-on, the baryonic matter interacted, while the dark non (or weakly) interacting mass contribution passed trough each other. This was observed by gravitational lensing, which revealed the true gravitational

field, as shown in Fig. 3.

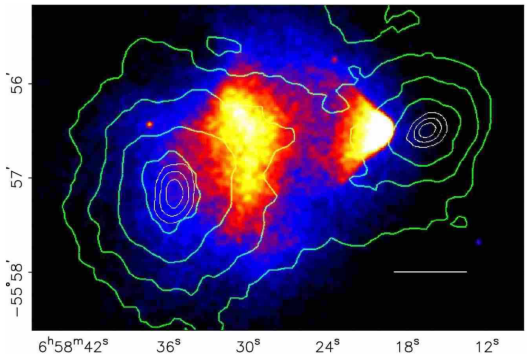

Figure 3: In green the mass distribution according to gravitational lensing with the distribution of the baryonic matter contained in the gas indicated in the color map from blue to yellow, which was determined using the x-ray emission from the gas [6].

In addition to the experimental evidence there is also a place for DM on the theoretical side. DM is one of the key components in the lambda cold dark matter (ΛCDM) model. It describes the evolution of the Universe from shortly after the Big Bang to the present day. It is based on the principles of the Big Bang theory and incorporates the ideas of dark matter and dark energy. According to the ΛCDM model, the Universe began with a period of rapid expansion known as inflation, which lasted for a tiny fraction of a second. This was followed by a period of radiation domination, when the Universe was filled with high-energy particles such as photons and neutrinos. As the Universe cooled down, matter particles such as protons and neutrons began to form, eventually leading to the formation of atoms and the creation of the cosmic microwave background (CMB) radiation. The presence of DM plays an important part in the spectrum of the CMB and allows for the prediction of the observed density fluctuations in the anisotropy spectrum [1].

1.2 Candidates

Dark matter is predicted to interact at most weakly with baryonic matter and should be electrically neutral, since a higher electric charge would lead to an increased interaction of DM and baryonic matter and thereby altering the structure formation and density fluctuations in the CMB. In addition, DM could not only interact with baryonic matter but also with itself. A non-vanishing self interaction

could explain the small-scale structure formation, but this cross-section is limited by the observations of merging clusters. Furthermore, DM should be long-lived compared to cosmological timescales [1].

One of the favored DM candidates are weakly interacting massive particles (WIMPs). They are predicted to be in the mass range of 1 to 10^5 GeV with an interaction cross section from 10^{-41} to 10^{-51} cm^2 based on different models. These particles candidates are non-relativistic and also electrically neutral [7]. Other candidates include axions, which arise as a solution to the strong CP problem. The origin is the spontaneous breaking of a global U(1) symmetry. In addition to addressing the strong CP problem, axions possess attributes that make them plausible DM candidats. They are very light compared to WIMPs (m $<$ 0.01 eV) and most importantly they would at most interact weakly with ordinary matter [8]. Apart from those two prominent candidates there are many other predictions, for example sterile neutrinos, which will be discussed in section 2 or dark photons, which are described in Ref. [1].

1.3 Experiments

In the field of physics, there are three primary methods to search for particles: production, indirect detection, and direct detection. Despite extensive efforts, none of these methods have yet observed a clear signal of DM. Nevertheless, it is important to continue exploring different experimental approaches in order to better understand this phenomenon [1].

Production

In the past, many particles from the Standard Model (SM) of particle physics have been detected using particle production, leading to the hope that DM particles could also be produced in a similar manner. The basic idea is that, since DM particles are predicted to interact with SM particles, it should be possible to create them in high-energy collisions. However, due to their weak interactions, DM particles would likely not be detected directly by the trackers and calorimeters used in accelerator facilities. To address this issue, a commonly used technique is to detect missing momentum in the collision events.

Using this technique, scientists searched for DM production in proton-proton collision at the LHC by probing mono-X signatures. A limit on the cross section was set, which constrains the potential production rate of DM particles [9]. It should be noted that direct comparisons between results from accelerator experiments and direct detection experiments are not straightforward due to the significant differences in the interaction processes involved, and therefore require careful interpretation [6].

Indirect Detection

Indirect detection methods aim to identify signals generated by annihilation or decay processes of DM particles [1]. The expected signal can take the form of gamma rays, neutrinos, or antimatter particles.

To search for gamma rays produced from DM processes, space- and ground-based telescopes such as Fermi-LAT [10] and HESS [11] are utilized. These experiments look for a gamma ray flux that exceeds the predictions of the SM. Dark matter can also accumulate in celestial bodies, where annihilation processes produce particles such as neutrinos. Neutrinos resulting from DM annihilation can be more energetic than solar neutrinos due to the lower mass constraint of DM. Searches for these neutrino fluxes are carried out by experiments such as IceCube [12] and ANTARES [13]. Another approach is to look for charged particles resulting from DM annihilation, such as positrons or antiprotons. The focus here is to achieve a high signal-to-noise ratio. Experiments that are centered around these searches include PAMELA [14] and AMS-02 [15].

Direct Detection

Direct detection aims to directly measure the interaction of SM particles with DM. This interaction is predicted to be an elastic scattering with an atomic nucleus, producing a signal in the form of light, charge, or heat. Additionally, a DM-nucleus scattering could displace an atom from the lattice in a crystal, which can result in the creation of a color center. This signature is further discussed in section 3.1.

Dark matter interactions in the realm of direct detection are categorized into two types: spin-independent (SI) and spin-dependent (SD). In SI interactions, all nucleons contribute coherently. Meanwhile, SD interactions involve consideration of nuclear spin from protons and neutrons [1].

Many direct detection experiments use two out of the three mentioned signals (light, heat and charge) in order to distinguish signals from background. One of them is the XENONnT experiment located at the Gran Sasso National Laboratory [16]. Together with several other collaborations, they set exclusion limits on the WIMP interaction cross-section at different masses (see Fig. 4).One of the limitations in direct detection experiments is the energy threshold for which a recoil can be observed, which makes the search for lighter WIMPs more challenging. PALEOCCENE could be suitable to probe the mass range in from 0.3 - 3 GeV. Details about this method is elaborated on in section 3.

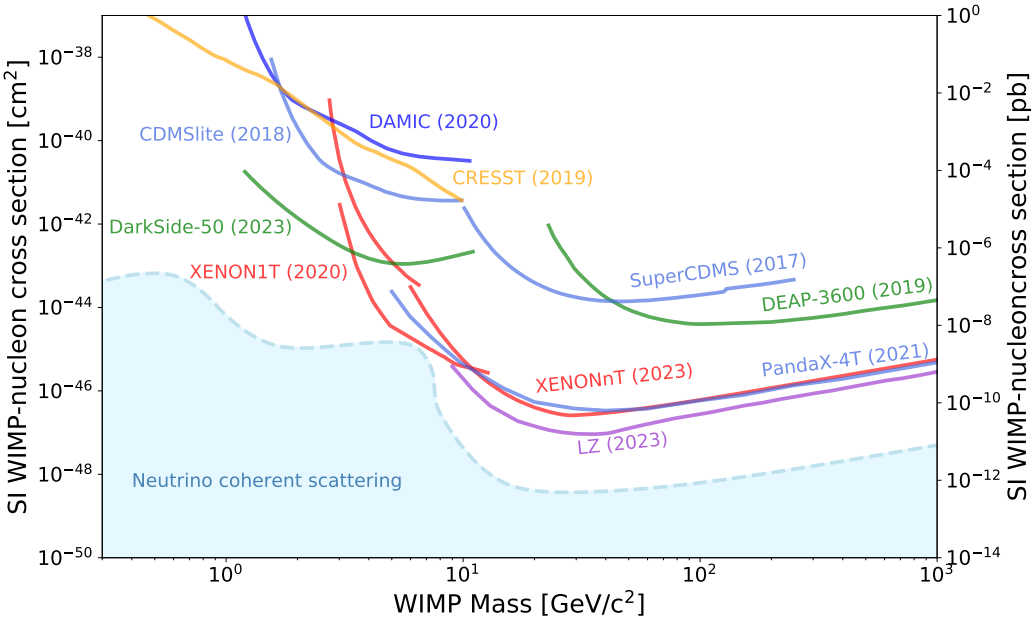

Figure 4: Spin independent DM cross section exclusion limits. The DM mass region above 2 GeV is well covered while the parameter space below this value remains fairly uncovered. In blue we see the neutrino floor, where an interaction from DM can not be distinguished (in an event-by-event basis) from coherent elastic neutrino-nucleus scattering (see section 2) induced by solar neutrinos, atmospheric neutrinos or the diffuse supernova neutrino background [17]. Graph kindly provided by Prof. Dr. L. Baudis.

2 Neutrinos

In our Universe, some of the most mysterious yet fundamental elements are neutrinos. They are elusive particles that effortlessly pass through matter, rarely interacting, yet carrying essential information about the cosmos. These particles, initially proposed to maintain equilibrium in nuclear reactions and subsequently observed in experiments, challenge our understanding of particle physics and cosmology. In this chapter, we introduce the unique characteristics of neutrinos and their role in the SM of particle physics.

2.1 Neutrinos in the Standard Model

The SM is a theory in particle physics that describes three of the four known fundamental forces (the electromagnetic, the weak, and the strong interactions), and classifies all known elementary particles. It is a quantum field theory, which was developed throughout the mid to late 20th century and has been remarkably successful in predicting experimental results. At its core, the SM classifies the elementary particles into two types: fermions, which make up matter, and bosons, which mediate the forces between fermions. Fermions are subcategorized into six leptons and six quarks, while bosons are divided into four types: the photon, the W and the Z bosons, and the gluon. The Higgs boson, discovered in 2012 [18], is an additional scalar boson, which gives other particles masses via the Higgs mechanism.

Fermions, obeying the Pauli Exclusion Principle, are subject to Fermi-Dirac statistics and have half-integer spins. Quarks interact through all three of the SM forces and group together to form hadrons, such as protons and neutrons. Leptons, which include electrons, muons, tau particles, and neutrinos, interact only through weak and electromagnetic forces (excluding neutrinos, which only interact through the weak force). Gauge bosons mediate the SM forces. Photons, massless and chargeless, mediate the electromagnetic force between charged particles. W and Z bosons, carrying a positive/negative and a neutral charge, respectively, mediate the weak force, which is among other things responsible for radioactive decays. Gluons, also massless and free of electric charge, mediate the strong force, which binds quarks

together in hadrons.

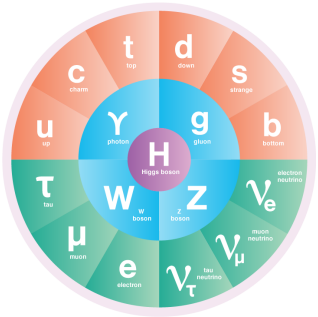

Figure 5: Overview of the particles in the SM. In orange are the quarks, the green color is for lepton, blue belongs to the force carriers, and purple is the higgs boson. An interactive version of this chart can be found at [19].

Neutrinos, which belong to the family of leptons, are elementary particles that are neutral in electric charge and haven an extremly small mass ($m_{\nu_e} < 0.8$ eV [20]) and interaction cross sections. They come in three types, or flavors: the electron neutrino, muon neutrino, and tau neutrino, such that each of these neutrino flavors is associated with a charged lepton.

A particularly interesting characteristic of neutrinos is their ability to oscillate between these flavors as they propagate through space. This phenomenon, known as neutrino oscillation, explained the shortfall in the detection rate of solar neutrinos, the solar neutrino problem [21]. The original formulation of the SM assumed that neutrinos were massless, much like photons. However, for neutrinos to oscillate between flavors, they must have different masses, because the oscillation depends on the differences in the squares of their masses. This discovery, confirmed by the Super-Kamiokande [22] and Sudbury Neutrino Observatory (SNO) [23] experiments.

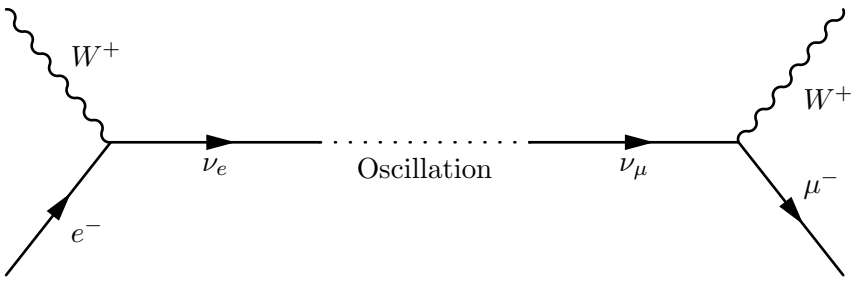

Figure 6: Feynman diagram of a neutrino oscillation process where an electron neutrino oscillates into a muon neutrino.

Neutrinos also play key roles in astrophysics and cosmology. They are produced in huge amounts in the sun and other stars, in supernova explosions, and during the formation of neutron stars and black holes. Despite the progress that was made in understanding these particles, many mysteries remain. For instance, we do not yet know the absolute masses of neutrinos and if there is another class of neutrinos, known as sterile neutrinos, which would only interact via gravity. Also unknown is whether neutrinos are their own antiparticles, a quality that would have profound implications for our understanding of the Universe, possibly explaining why there is more matter than antimatter in the Universe. By studying neutrinos, we can not only refine the SM and enhance our understanding of fundamental particles, but we might also shed light on unresolved questions in physics and cosmology [1].

2.2 Coherent Elastic Neutrino-Nucleus Scattering (CEνNS)

The interaction of neutrinos with matter includes a variety of processes, among which Coherent Elastic Neutrino-Nucleus Scattering (CEνNS) holds a particular position. First predicted by Daniel Freedman in 1974 [24], CEνNS is a process where a neutrino scatters off an entire nucleus, which recoils as a whole, rather than interacting with individual nucleons. The key condition for the coherence in CEνNS is that the momentum transfer must be small enough that the neutrino's interaction remains coherent across the entire nucleus, a criterion met when the exchanged momentum is less than the inverse of the nuclear size [25]. This leads to a prediction of a relatively-low-energy nuclear recoil spectrum, typically below a few tens of keV, and thus challenging to detect.

CEνNS, being a neutral-current process, is flavor-independent, meaning that it occurs with equal probability for electron, muon, and tau neutrinos and their antiparticles. This is due to the Z boson, mediator of the weak neutral-current interactions, which couples to all neutrino flavors equally. As a result, CEνNS provides an opportunity to probe the weak neutral-current interaction, and due to its coherent nature, the cross-section scales approximately with the square of the number

of neutrons in the nucleus. Despite its theoretical prediction over four decades ago, the observation of CEνNS remained elusive due to the experimentally challenging nature of detecting low-energy nuclear recoils. It was only in 2017 that the COHERENT collaboration reported the first observation of CEνNS at the Spallation Neutron Source (SNS) at Oak Ridge National Laboratory. Utilizing a CsI[Na] scintillator and exploiting the high-intensity, well-known neutrino source provided by the SNS, the COHERENT experiment marked a significant milestone in neutrino physics [25].

The detection of CEνNS opens an avenue to a multitude of research directions, from precise tests of the SM to searches for new physics. For example, the NUCLEUS experiment tests the weak mixing angle and has the potential to contribute to beyond the SM (BSM) physics by measuring the cross-section for CEνNS using $CaWO_4$ and Al_2O_3 calorimeter arrays [26]. Moreover, CEνNS has implications in the field of astroparticle physics. Neutrinos produced in supernovae would predominantly scatter via CEνNS in DM-detectors. Therefore, detailed understanding of this process is crucial for interpreting signals for future supernova detection. Given that a CEνNS interaction results in a recoiling nucleus, which is also the outcome expected from WIMP scattering with matter, techniques developed for CEνNS detection could be repurposed for dark matter searches [27].

The study of CEνNS serves as a tool for investigating a range of phenomena in particle and astroparticle physics. Future improvements in detector technologies and experimental methods, as well as the deployment of detectors in a variety of environments, promise to expand the scientific reach of CEνNS in the coming years.

2.3 Reactor Neutrinos

One of the key sources of neutrinos is nuclear reactors. Nuclear reactors produce neutrinos as a byproduct of the fission process used to generate energy. As such, they have been a crucial tool in the study of neutrino physics and have provided some of the most precise measurements of neutrino properties. When a neutron-rich nucleus undergoes fission in a reactor, it splits into two smaller, neutron-rich fragments. These fragments undergo beta decay, where a neutron decays to a

proton by emitting an electron and an electron antineutrino. The antineutrinos produced in these reactions are what we refer to as reactor neutrinos. The high-intensity, fairly-understood flux, and the energy spectrum of these antineutrinos make them an excellent probe for studying the properties of neutrinos and testing the predictions of the SM [28].

Reactor neutrino experiments have made significant contributions to our understanding of neutrinos. The Kamioka Liquid scintillator AntiNeutrino Detector (KamLAND) experiment in Japan made a decisive observation of neutrino oscillation by measuring the depletion in the flux of electron antineutrinos at long baselines (distances of the order of 100 km). Further, Daya Bay [29] and Double Chooz [30] precisely measured the value of the mixing angle Θ_{13} by comparing the flux and the spectrum of electron antineutrinos at near and far detectors. Additionaly, there are many experiments attempting to detect CEνNS originating from reactors. For example CONUS [31] and MINER [32] use cryogenic germanium detectors, whereas RICOCHET [33] and NUCLEUS [34] employ bolometers. These experiments all operate at temperatures in the range from a few mK up to 170 K [35]. Alternatively, an approach for a detector working at room temperature is shown in the next chapter [36].

The detection and monitoring of reactor neutrinos not only aids in our understanding of fundamental particle physics but also has important applications for nuclear safety and non-proliferation. The sheer number of neutrinos produced in a nuclear reactor and their penetrating ability make them an ideal tool for monitoring nuclear activity. This includes tasks such as verifying the operational status of reactors, assessing the type of fuel being used, and even detecting secret nuclear activities. Since each fission event in a nuclear reactor produces approximately eight neutrinos, the operational status of a reactor and its power output can be inferred by monitoring the neutrino flux. An increase or decrease in neutrino flux corresponds to a change in the reactor's power level. Thus, remote neutrino detectors could potentially serve as a method to independently verify a reactor's operational status [28].

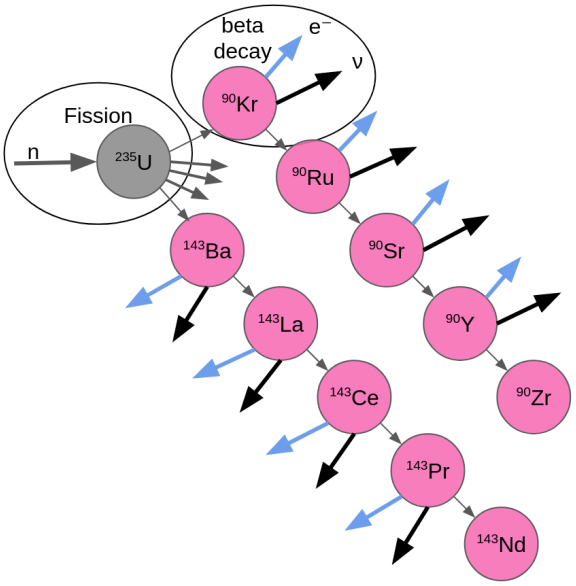

Figure 7: Example of a fission process showing the fission fragments including the decay chain, which produces eight neutrinos. Figure adapted from [28].

In principle, a sufficiently sensitive neutrino detector could detect a hidden nuclear reactor or even a nuclear explosion from great distances. It is important to note, however, that practical implementation of neutrino-based nuclear monitoring faces several challenges. Current neutrino detectors are complex and expensive, as a large size is often necessary to achieve a useful detection rate [28].

3 PALEOCCENE

The PAssive Low Energy Optical Color CEnter Nuclear rEcoil (PALEOCCENE) concept represents a method for the detection of low-energy nuclear recoil events. Unlike conventional systems, which require restricting operational conditions (such as high voltage, a vacuum, or cryogenic temperatures), PALEOCCENE detectors are designed to operate passively at room temperature, making them suitable for a wide range of applications. To fully realize the potential of this concept, a multi-disciplinary collaboration of experts in particle physics, solid-state physics, nuclear physics, dark matter detection, and nuclear engineering was formed [37].

The principle underlying the PALEOCCENE detection concept lies in the process that takes place when a nucleus experiences a recoil. In scenarios where the energy transferred during the recoil process exceeds the binding energy of a crystal atom, the atom may be dislocated. This can lead to a permanent vacancy in the lattice if the atom is displaced far enough, such that it cannot recombine and return to its original place, usually within a distance of 1-2 nm. The recoil energy required for the creation of a permanent vacancy typically lies in the range of 20-200 eV, a threshold also known as the Threshold Damage Energy (TDE). The TDE depends on the direction of the incoming particle. This could give directional information, which would help to reduce backgrounds in CEνNS detections aand DM detection [37].

Neutrons are the most significant background source, originating from cosmic rays, fission, as a result of muon-induced interactions or in (α,n)-reactions. Since PALEOCCENE uses passive detectors, it is not possible to use an active muon veto in this detection approach to reduce the background. In addition, gamma-rays can result in background events. In the context of PALEOCCENE, these gamma-ray induced background may be strongly dependent of the type of target and necessitate further research since there is only a limited amount of literature available on this topic to date [37].

The theoretical DM cross-section exclusion limit that could be achieved with a

PALEOCCENE detector is shown in Fig. 8. PALEOCCENE could provide the best limits for the spin-dependent cross section in the DM mass range from 0.3 to 3 GeV using a 10 g-yr exposure of a LiF crystal. However, this is only true for spin-dependent interactions, as there are superior detectors sensitive to low-energy nuclear recoils induced by spin-independent interactions such as DAMIC [38] or SuperCDMS [39]. This spin-dependency can be achieved by using a target material that has components with a non-zero net spin. In the case of LiF both components have a net nuclear spin of 1/2.

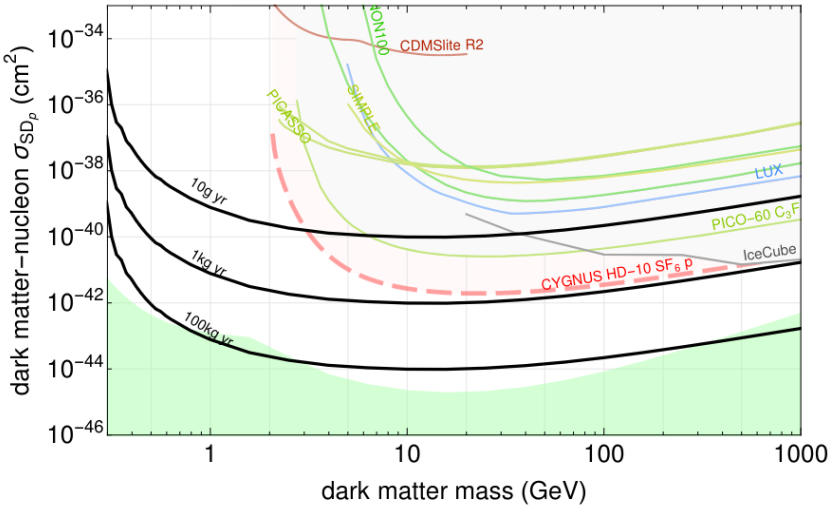

Figure 8: 95% confidence limit in black for the spin-dependent DM cross-section for a LiF PALEOCCENE detector without considering backgrounds. In green we can see the neutrino floor for LiF. Figure taken from [37]

In the context of PALEOCCENE, the role of color centers, specifically F-centers, is crucial. An F-center is essentially an anion vacancy in an ionic crystal that captures an electron. The intrinsic nuclear recoil detection threshold is set by these centers, as their formation energy is around a few tens of electronvolts. More information on color centers is given in section 3.1. Notably, the detection strategy of PALEOCCENE employs light sheet microscopy, or more precisely, Selective Plane Illumination Microscopy (SPIM). This technique allows for the optical detection of single color center fluorescence in extensive bulk volumes (section 3.2).

Considering the occurrence of color centers across a broad spectrum of materials, it appears plausible that a range of detector targets could be suitable for the

PALEOCCENE approach. Nevertheless, choosing the appropriate material for effective detection is crucial. Such material candidates should demonstrate properties including a high melting point, behave as an electrical insulator, permit optically active defects predominantly formed by nuclear recoils, be available in optical quality crystals, contain high-mass elements, have a low TDE, and possess an F-center absorption and emission spectrum in the visible range. Promising material candidates include LiF, BaF_2, NaI, CsI, $CaWO_4$, $Bi_{12}GeO_{20}$ (BGO) and CaF_2, which exhibit favorable characteristics for this detection concept [37]. The response of NaI can be seen in Fig. 9, which displays the simulation of cosmic ray neutrons and CEνNS events. NaI is also the material that could be used in the search for CEνNS originating from reactor neutrinos. With a 10 g-yr exposure of a NaI crystal at a 20 m distance from a 3 GW_{th}[1] reactor, it should be possible to detect a CEνNS signal at 5 σ [36].

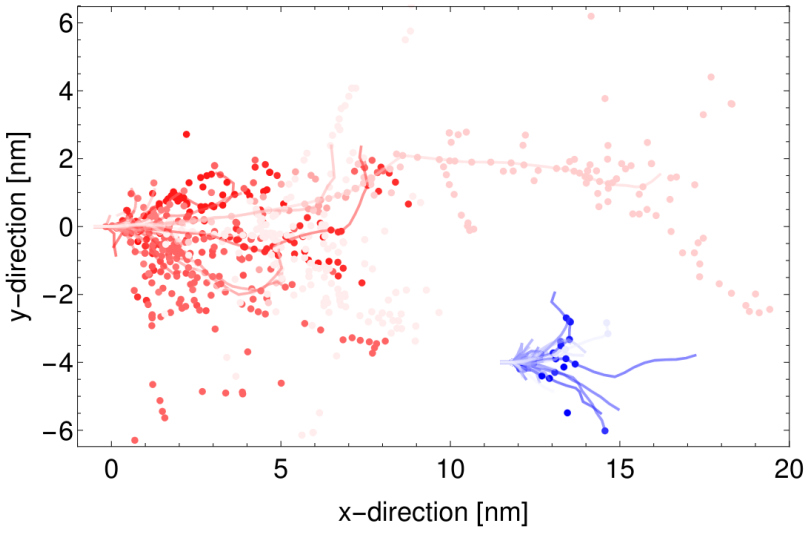

Figure 9: Simulated color center formation in NaI. The lines indicate the paths with primary recoils and the dots mark the created vacancies. In red is the overlay of 50 cosmic ray neutrons and in blue are reactor CEνNS events. Figure taken from [37].

3.1 Color Centers

Imperfections and irregularities within the crystal lattice can lead to fascinating material properties and rich physics. In this chapter, we will discuss color centers,

[1]Total amount of heat energy produced by the reactor core. It includes the energy that is converted into electricity as well as the energy lost as waste heat.

their underlying physics, types, and the mechanisms of their formation.

Color Centers and the Underlying Physics

The research in this topic began in the 1920's, when it was observed that alkali halide crystals can be colored through irradiation with X-rays [40]. The irradiation causes point defects, which can result in color centers. The fundamental concept of a color center revolves around the behavior of electrons. In a defect-free crystal, electrons occupy states in well-defined energy bands. The lower-energy band is known as the valence band, while the higher-energy band is known as the conduction band. The gap between these two bands is referred to as the bandgap. A change in the crystal structure can create a localized energy level or levels within the bandgap. An electron can be trapped in this localized state, resulting in a color center [41].

These trapped electrons can absorb photons with energy equal to the energy difference between the ground state and an excited state. This absorption process corresponds to the electron being excited from the ground state to the excited state. Subsequently, when the electron relaxes back to the ground state, a photon is re-emitted, a process known as photoluminescence (PL). The energy (and hence the color) of the emitted photon corresponds to the energy difference between these states. Therefore, the color that a material with color centers exhibits is inherently related to the energy levels of the centers [41]. For PALEOCCENE an additional important consideration is the response to annealing and bleaching. The former describes the self healing process of the crystal when exposed to sufficiently high temperatures and the latter depicts the process of color centers losing their optical activity due to exposure to light [37].

Different Types and Their Formation

There is a wide array of color centers that can form in various materials, each with unique properties and formation mechanisms. A few are listed as follows, whereas more information can be found in Ref. [40]. Formation of color centers can be achieved through various processes such as high-energy irradiation or controlled

annealing processes, which create vacancies or interstitials in the crystal lattice [40]. PALEOCCENE focuses on the formation of color centers through irradiation, but has to consider that there are other methods, that can lead to these fluorescing crystal defects.

- **F-Centers** Perhaps the simplest form of color centers, F-centers (from the German word 'Farbe' meaning color), occur when an anionic vacancy in a crystal lattice captures a free electron. This type of center is often observed in alkali halide crystals where the crystal lattice is missing a negatively charged halide ion [41].

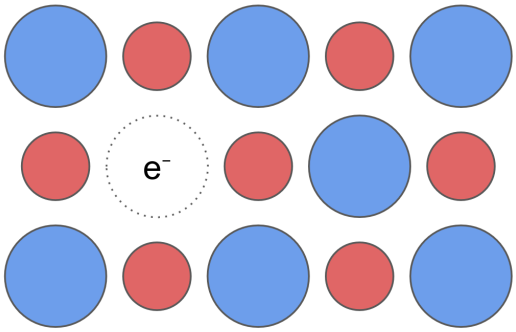

Figure 10: Sketch of the F-center, which is a negative ion vacancy, which is occupied by a single electron. Negative ions are blue and positive ions red. Figure adapted from [41].

- **F^--Centers** They are similar to the F-center but with two trapped electrons in the same vaccancy [40].

- **M-Centers** This type of color center appear when two F-centers are in neighbouring locations. Therefore, they are also called F_2-centers in some literature [41].

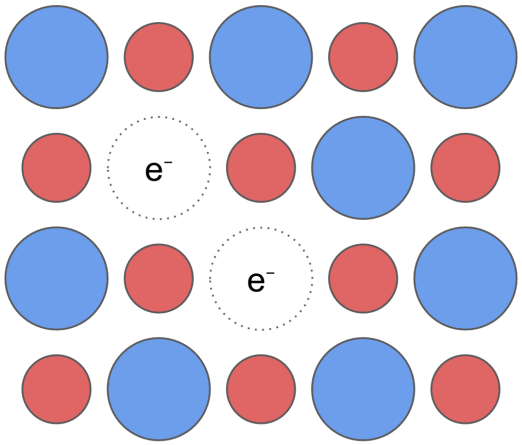

Figure 11: Schematic drawing of an M-center, which consists of two adjacent F-centers. Figure adapted from [41].

- **V_k-Centers** They form when a hole is not occupied by an electron but by a pair of negative ions [41].

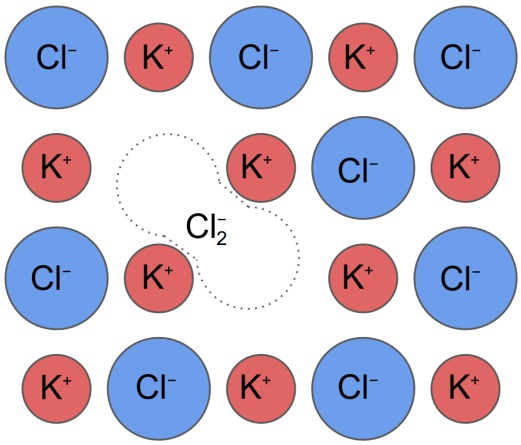

Figure 12: Schematic drawing of a V_k-center in KCl. A Cl_2^- ion occupies the vacancy of a missing Cl^--ion. Figure adapted from [41].

- **Nitrogen-Vacancy (NV) Centers** Being one of the most extensively studied color centers, NV centers occur in diamond when a nitrogen atom substitutes a carbon atom in the lattice, adjacent to a carbon vacancy [40].

3.2 Light Sheet Fluorescence Microscopy

Light sheet fluorescence microscopy (LSFM), also known as selective plane illumination microscopy (SPIM), is a powerful imaging technique, which has gained significant popularity in the field of biological research. It was first introduced in

the early 2000s and has since revolutionized the visualization and study of living organisms [42].

The fundamental principle of LSFM is the use of a thin sheet of laser light, which illuminates a small section or 'plane' of the specimen at a time. This light sheet is perpendicular to the direction of observation, allowing for optical sectioning and reducing the amount of light exposure to the specimen. This is a significant advantage over traditional fluorescence microscopy techniques, which often expose the entire specimen to light, leading to photobleaching. The technique is especially useful for long-term imaging of developmental processes in living organisms, as it allows for the observation of structures and processes in three dimensions over time [42] and is now taking a leap into the domain of particle physics.

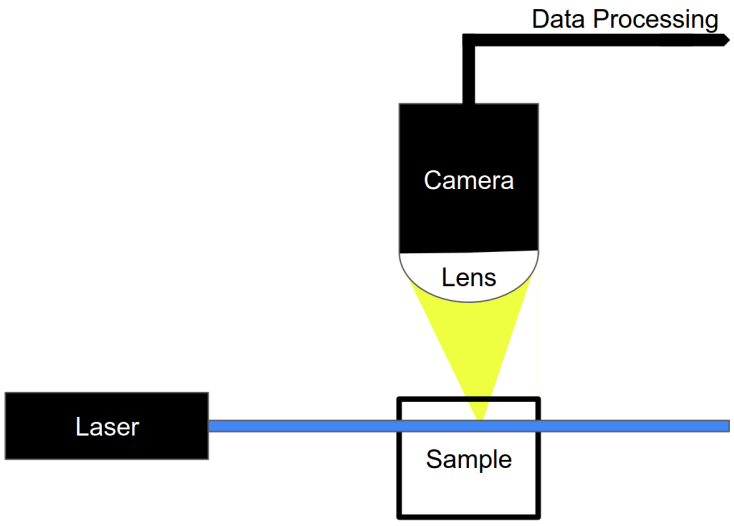

Figure 13: Schematic drawing of the light sheet microscopy principle. The incoming light triggers the photo luminescence inside the sample, which will be collected by the lens and then recorded by the camera.

4 Samples and Measurements

In this section, we will discuss the samples used for data analysis and describe the light sheet microscopy setup at the University of Zurich (UZH), known as mesoscale selective plane-illumination microscopes (mesoSPIM). We will cover the reasons for choosing the samples, their properties, and preparation methods. Additionally, we will explain the functionalities and key components of the mesoSPIM setup. Understanding the samples and the mesoSPIM setup is important for interpreting the collected data and experimental results.

4.1 Samples

For the initial PALEOCCENE studies, it was essential to select suitable materials. Based on the proposed criteria in section 3, CaF_2 was chosen, because it possesses several beneficial attributes: it is readily available in optical quality from vendors, has an intermediate atomic mass, its excitation and emission wavelengths are in the visible spectrum, and there is a good theoretical understanding of its threshold damage energy, determined via molecular dynamics simulations [43]. In order to validate the proposed detection method and establish a correlation between neutron dose and spectroscopic signals, experimental trials were conducted using neutron sources. CaF_2 samples were exposed to neutrons from a 10 mCi ($3.7 \times 10^8 Bg$)AmBe source at a fluence of up to 10^8 n/cm^2. Using spectroscopy, collaborators observed a clear increase in photo luminescence (PL) for irradiated samples [37]. This aligns with our expectations and offers a promising starting point for further investigation with light sheet microscopy.

Hence, CaF_2 was chosen for the first analysis with the mesoSPIM at UZH. There are five cubic crystals with a volume of 1 cm^3. The samples were acquired from two vendors (*Crystran* and *United Crystals*) and have in common that all of the sides are polished to reduce multiple scattering of the light inside the sample.

- **Crystran** Three CaF_2 samples were ordered from *Crystan* (see Fig. 14). One was not irradiated, which will be also referred to as a 'blank' sample. The remaining two were irradiated at Penn State University using a ^{60}Co

source, which produces photons with energy emission peaks at 1.17 MeV and 1.33 MeV [44] and is expected to create a uniform energy deposition inside the crystal. The received dose for the crystals are 10^5 Rad and 5×10^6 Rad. These samples are named according to their irradiation dose, *blank*, *100 kRad* and *5 MRad*.

- **United Crystals** The two samples from *United Crystals* are named *VT303* and *VT306*. *VT303* was irradiated at Virginia Tech with neutrons provided by an AmBe source with a flux of 10^8 n/cm^2. *VT306* was left blank.

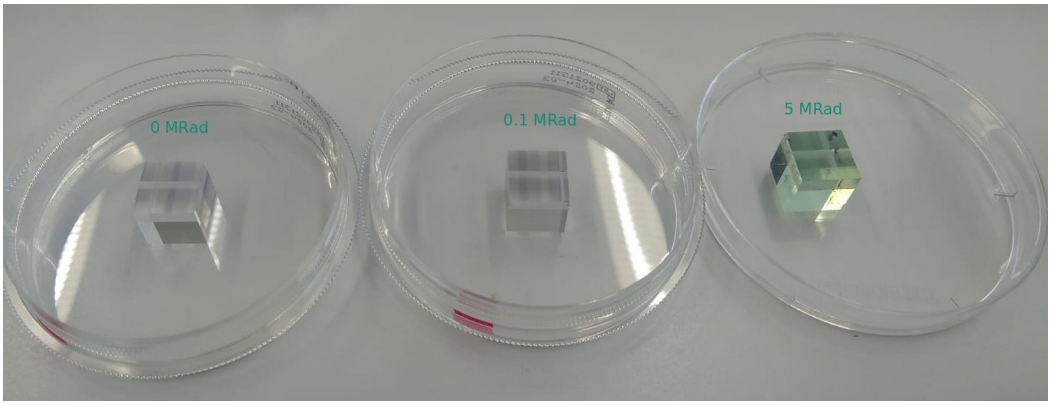

Figure 14: The three samples from *Crystran*. On the left is the *blank* sample, in the middle the *100 kRad* sample and on the right the *5 MRad* crystal, which turned green due to the irradiation.

4.2 Measurement

The data for this project was taken using two different mesoSPIM at the University of Zurich. The mesoSPIM is an open-hardware project developed to address the challenges in imaging cm-sized cleared samples with near-isotropic resolution within minutes [45].

Alternative light sheet microscopes typically have limitations, either by being suitable only for smaller-sized samples or by attaining the best image quality exclusively within a specific region. The mesoSPIM addresses these challenges by offering a light sheet microscope that combines a large imaging volume, excellent image quality over a large field of view with simple and versatile sample handling [45]. The upgraded mesoSPIM, also referred to as 'Benchtop' mesoSPIM, offers improved

resolution[2] and a significantly increased field of view, and higher throughput compared to the original version[3] [46].

Fig. 15 shows a schematic of the measurement procedures using the mesoSPIM light sheet microscope. There are several adjustable parameters for the scanning procedure. The most important for this thesis will be explained in the following.

- **Excitation Light** The PL is triggered using a laser. Thereby one can chose between four different wavelengths, which are 405 nm, 488 nm, 561 nm and 640 nm. All these lasers have a power of 100 mW and can be adjusted in intensity [47].

- **Emission Light Filter** The emitted light can be filtered, such that photons with certain wavelengths do not reach the camera. This can be used to reduce the contribution from scattered light and therfore help to detect the luminescent features. The choice of the filter can be made between three long pass filters (515 nm, 561 nm and 594 nm), which block all light with shorter wavelength and a quadband filter, which removes the wavelenghts 405 nm, 408 nm, 561 nm and 640 nm. It can be noticed that the quadband filter eliminates the wavelength of the excitation light, which reduces the contribution from scattered light to the recorded signal [47].

- **Magnification** With specific lenses the magnification can be enhanced. Typical magnification factors which are used for the data taking are: 0.8, 1.0, 1.6, 2.0, 4.0, 6.3, 10.0 and 20.0.

- **Step Size** The distance between two consecutive planes is called the step size. For our scans this adjustable value is in the range from 3 - 10 μm.

- **Galvo Amplitude** The galvo amplitude determines the area covered by the light sheet. In most of the scans the galvo amplitude was chosen to cover only part of the recorded area, such that there is an illuminated and non illuminated region.

[2] Axial optical resolution improved from 5.0 μm to 3.3 μm and laterally from 2.7 μm to 2.0 μm [46].

[3] An overview of the differences can be found in table 1 in [46].

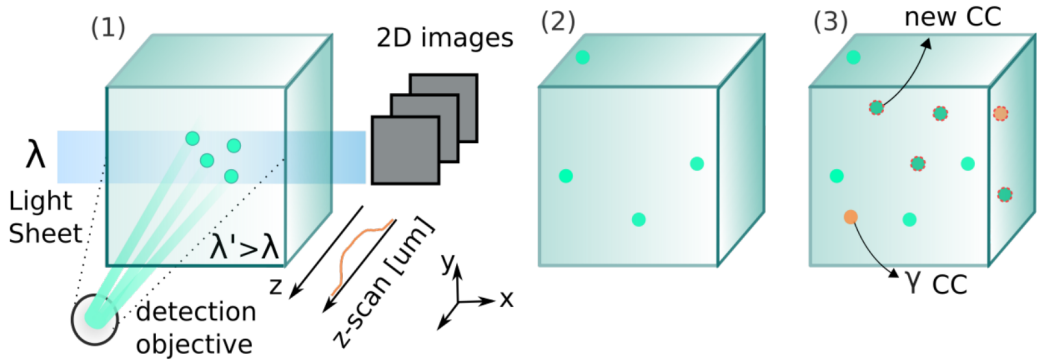

Figure 15: In LSFM, a thin light sheet illuminates a z-section of the sample x-y plane which is observed by a camera orthogonal to the light-sheet source (1). By incrementally shifting the sample along the z-axis, 3D images are generated. The scans acquired prior (2) and after the exposure (3) to a neutron or gamma source can be compared. Feasible target materials for nuclear recoils should yield none or distinct response to γ rays (3). Figure and caption taken from [48].

The cubic crystal is positioned in a custom-made holder produced to ensure precise alignment (see Fig. 16). It is important to arrange the front side of the crystal parallel to the incoming light from the sides. Aligning the sides perpendicular to the laser ensures that the light is not reflected multiple times, thereby yielding high-quality images and more reproducible dataset since the effects of refraction are minimized. Once the R&D phase is completed, we may deploy a crystal for an extended duration, during which regular scans will be conducted. In such instances, the precise determination of pixel position becomes vital[4]. This precision is especially useful for identifying pre-existing defects and color centers, as these must be known to ensure sensitivity to rare processes such as CEνNS or DM-nucleus scattering. Currently, the alignment process is done manually by focusing the laser inside the crystal while adjusting the sample position and mesoSPIM settings, as described in [48].

[4]To ensure this in the future, there are plans to utilize markers on the surface of the crystal.

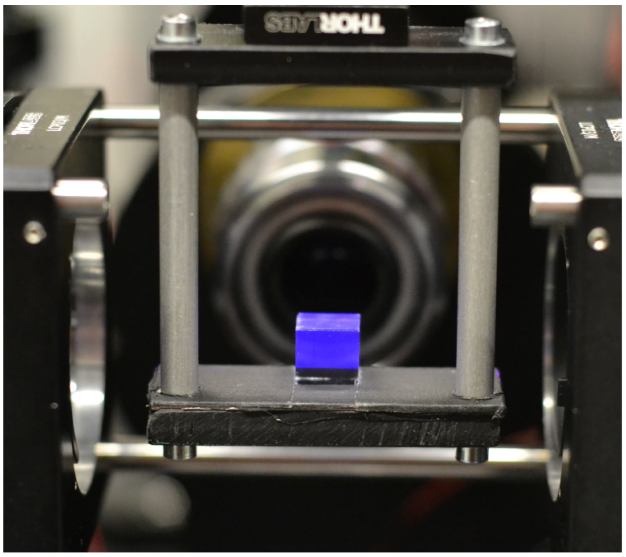

Figure 16: Picture of a CaF_2 crystal in the mesoSPIM. The crystal shines blue due to the laser light coming in from the side. Behind the sample in the background the camera can be seen [46].

The scans are saved on the servers from UZH in the form of Tagged Image File Format (.tiff) or in Hierarchical Data Format (.h5), where each file contains around $\mathcal{O}(10)$ GB of data. The data in the files is structured as three-dimensional arrays, where the first index selects the plane and the remaining two the column and row. Each entry, also called pixel, has an assigned intensity value from 1 to 65536 (16 bits). Although a larger intensity indicates more photons reached the given pixel, the pixel intensity value does not directly correspond to the number of photons detected by the camera, nor provides information about the photon's wavelength. In order to keep track of the conducted scans, a script was created as part of this work to read out the mesoSPIM scan setting files automatically generated for each acquired scan. These values are added to a spreadsheet on the UZH servers and synchronized with an external spreadsheet, where additional information and comments can be added.

It is noteworthy that the crystals are not perfectly clean, we often find dust particles on their surfaces (see Fig. 17). Interestingly, these dust particles aid in setting the focus due to their high visibility and brightness caused by the scattered light during the focusing process where no filter is used.

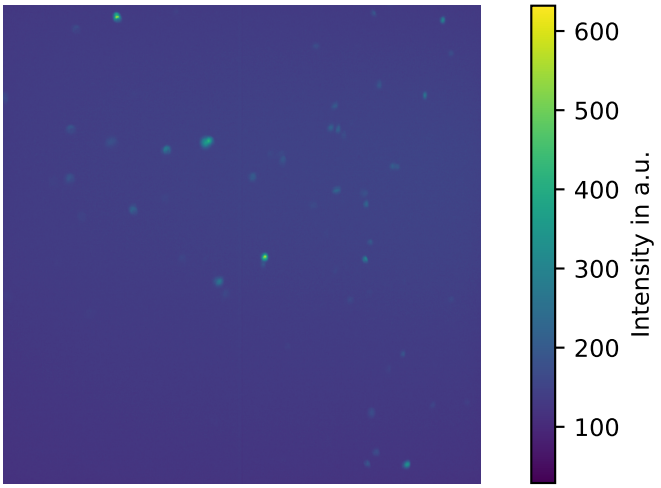

Figure 17: Surface dust seen as high-intensity spots with the mesoSPIM.

The dust on the front side of the crystal can have a notable effect on measurements. This dust can cast a 'shadow' in images inside the crystal, reducing pixel intensity and creating blind spots that prevent color center detection. These blind spots, however, are not entirely disadvantageous, their tracking can help estimate the crystal's tilt or misalignment through light refraction. This technique was employed in Fig. 18, where the tilt was estimated to be around 0.5 degrees.

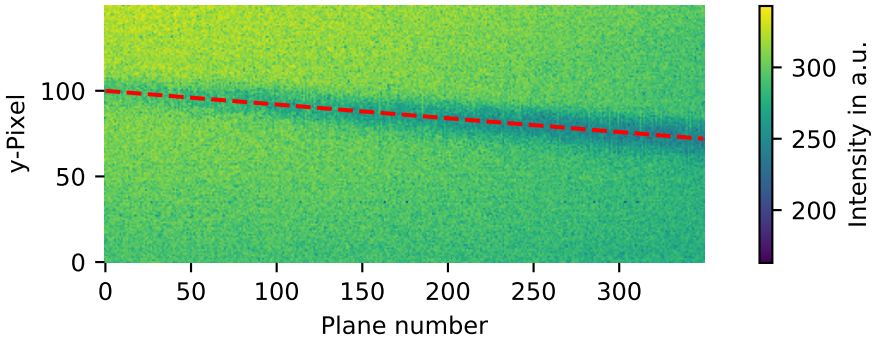

Figure 18: This image projects the minimal intensity around a dark spot, providing a side view of the crystal. The red line estimates the center of the dark spot caused by the shadowing effect from the dust on the crystal's surface.

5 Data Analysis

This chapter details the main work of the thesis. The goal of this project is to develop the first analysis methods for this new approach of detecting color centers induced by nuclear recoils, which could potentially find applications in DM and neutrino physics. Since at this stage PALEOCCENE is in the R&D phase, it is not yet the goal to find a signal of DM or neutrino events, but rather to investigate if this will be possible with the current setup at a later stage. Therefore, three main topics will be covered in this thesis throughout the next three sections, revolving around quantifying the fluorescent features in crystals scanned with the mesoSPIM.

- **Fiducialisation:** The fiducial volume represents the region which can be used for data analysis. In our case this is determined by the illumination effects, such as the high intensity which is observed near the surface of the crystal or the non-uniform illumination in individual planes. The corresponding section will evolve around the determination of this fiducial volume, which will be used for the remainder of the analysis.

- **Track Finding:** This method corresponds to the development and testing of a structure finding algorithm, giving insight to the possibility of detecting preexisting defects as well as enhance the understanding of color center formation. These elongated structures (around 10 - 40 μm) could have been formed by irradiating particles leaving behind color center tracks. Other causes include impurities or defects induced during the production and sample handling.

- **Pixel Matching:** In the last analysis methods development section we examine the data from repeated scans to detect high intensity pixel occurring at the same coordinates and is referred to as 'pixel matching'. Repeated scans are multiple data sets of the same crystal at the same location taken with exactly the same mesoSPIM settings. Pixel matching helps in ensuring that the mesoSPIM can precisely locate pixels with high intensity at consistent positions, which is vital for confirming the accurate formation of color centers.

The next sections will describe these methods using the data from the sample

100 kRad measured with both mesoSPIM setups (standard and benchtop). The relevant methods will be again applied to the specific case of neutron irradiated samples measured with the standard mesoSPIM in section 5.4.

5.1 Fiducial Volume

This section will explain the process of fiducialising the data. The goal of fiducialisation is to determine the crystal surfaces as well as the illuminated region within the bulk of the crystal. For this we need two kinds of fiducialisations:

- **x-y-fiducialisation:** The x-y-fiducialsiation determines the illuminated region in a plane. This is necessary because we do not illuminate the whole plane during data taking, which means we record illuminated and non-illuminated regions.
- **z-fiducialisation:** The scanning procedure is started outside of the crystal and subsequently the light sheet is moved into the material. Therefore we need to deterimine when the light sheet enters and leaves the crystal.

The illumination for the standard and upgraded mesoSPIM (see section 4.2) show a clearly distinct intensity profile, therefore this section is divided into two parts to discuss the data from the two mesoSPIM versions separately.

First, we start with general observations. As the light sheet traverses the crystal, the average intensity across individual planes changes. An observable trend is the increase in intensity towards the crystal's surface. This is attributed to the finite size of the light sheet, creating a continuous transition from outside to inside the crystal, in contrast to a delta-function shaped behavior.

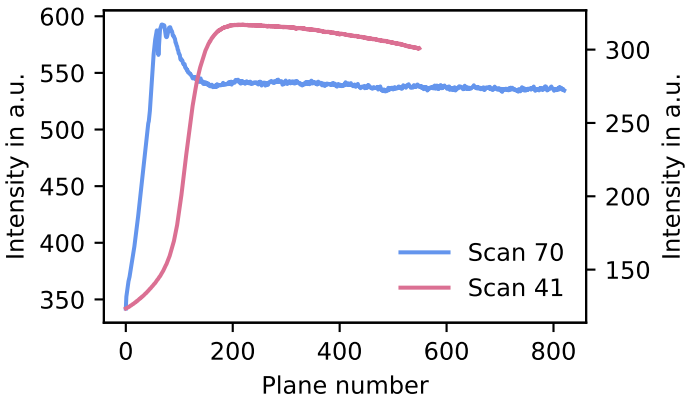

Figure 19: Comparison of average intensity profiles for two distinct scans of the same crystal (*100 kRad*). Scan 70 was taken with the upgraded mesoSPIM, and scan 41 with the standard one. Scan 70: the intensity increases at a higher rate within the crystal before falling to a plateau where it remains almost constant, which is an indication for a thinner light sheet. Scan 41: the average intensity increases towards and within the crystal before resulting in a steady decline.

At the boundary of the crystal, the intensity continues to rise, which might be due to the scattering of laser light by surface dust. Once inside the crystal, the behaviour of light intensity is more steady. There is a difference in the two versions of the mesoSPIM, probably due to a thinner light sheet in the upgraded version. This leads to a range of behaviors of average intensity, as showcased in Fig. 19.

An additional challenge that recurs in the analysis is the non-uniform illumination of the planes by the laser. While this might not be an issue for many mesoSPIM applications, for the PALEOCCENE project it is crucial to account for this inhomogeneity. The non-uniformity appears in Fig. 20 in the form of a gradual transition from illuminated to non-illuminated pixels and dark spots which are caused by the shadowing effect mentioned in the previous section.

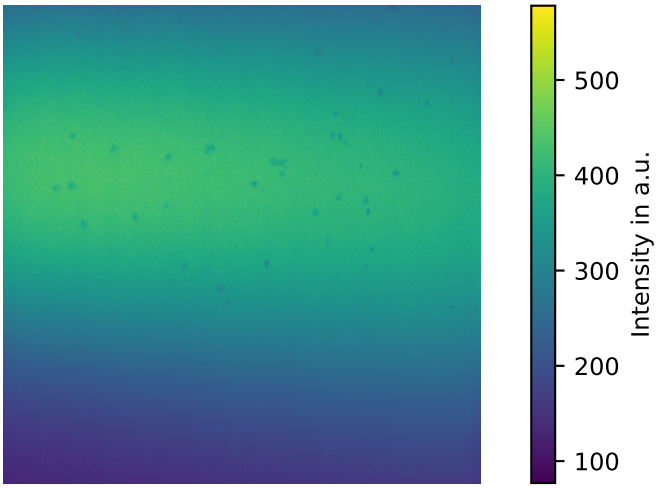

Figure 20: Dark spots induced by dust on the crystal surface, as shown in Figure 17. In addition, we can see the non-uniform illumination. The dark region towards the bottom was not illuminated by the laser.

Standard mesoSPIM

We start with the x-y-fiducialisation. In Fig. 21 the dominant peak on the left corresponds to non-illuminated pixels, which tails off into a smaller peak on the right, representing the center of illumination. The transition from the illuminated to non-illuminated region is gradual rather than abrupt, causing the tail connecting the two peaks[5]. This makes defining the fiducial volume more challenging.

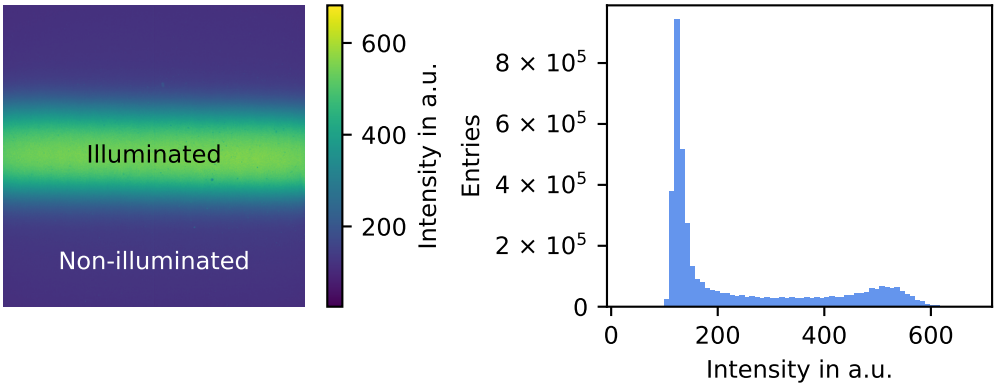

Figure 21: On the left is a plane from the scan of the *100 kRad* sample approximately 0.3 cm into the crystal. On the right is the corresponding intensity distribution.

[5]The intensity distribution inside a plane highly depends on the mesoSPIM settings, especially how well the light sheet is focused.

Due to the gradual transition, it is preferable to estimate the distribution from the non-illuminated part to set the boundaries between the two regions. This can be done in two ways: First, we can analyze the pixel intensity distribution of the planes before the laser interacts with the crystal. There, we are outside of the crystal and do not expect to see luminosity. The downside of this approach is the differing conditions inside and outside the crystal, which might be caused by scattering of the laser light. Second, the non illuminated pixel intensity distribution can be estimated using the region in the same plane, which is clearly outside the illumination. The disadvantage here is that we first have to define the region for calibration, which is linked to the various settings in the mesoSPIM.

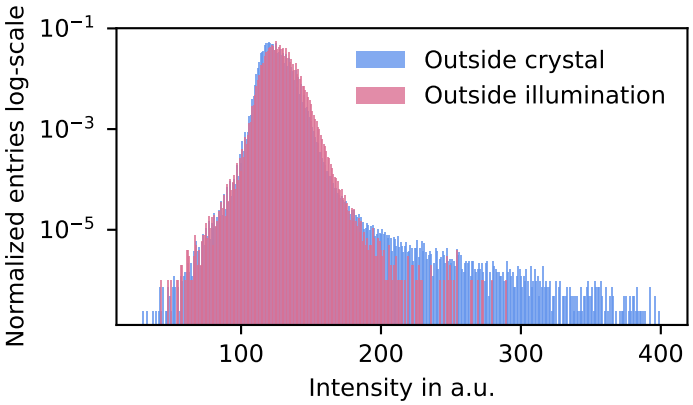

Figure 22: Histograms of the pixel intensities from different calibration regions, showing that there is no significant difference, except for the tail for the distribution of the intensities of the pixel that are recorded before the laser illuminates the crystal.

In Fig. 22 we see that the two distributions are very similar apart from the tail in the intensity distribution from the pixels recorded outside of the crystal. This tail can be attributed to pollutants on the crystal's surface scattering light towards the lense of the microscope. The advantage of using the intensity distribution outside the crystal is that there is more statistics and we do not need to care about the region of illumination. The drawback however is that there is pollution and the starting point of the scan has to be far away from the surface to avoid the previously discussed effects. The advantage of using the interior pixel intensity distribution is that there should be no pollution, but with the disadvantage that one has to be careful when dealing with different galvo amplitude and choosing the region where

no illumination is present. Nevertheless, once the scanning procedure is standardized this should be no problem. Therefore the intensity distribution from the region inside the crystal and outside the illumination[6] is chosen as a calibration source for determining the boundary.

A plausible approach for the fiducialisation involves defining two thresholds. The first specifies the intensity level where a pixel is identified as fluorescing, and the second indicates the minimum number of pixels per row or column that must exceed this threshold for a line of pixels to be considered illuminated by the laser. This strategy is particularly useful for samples with a high level of luminescence and less for a sample with little response to illumination, because there we cannot see the transition. However, this technique can be used for science data, where the PL is rare, in the following way: A highly luminescent sample, such as the sample *100 kRad*, is used to determine the boundaries. Afterwards we scan a sample which searched for rare events with the same mesoSPIM settings and apply the same fiducialisation.

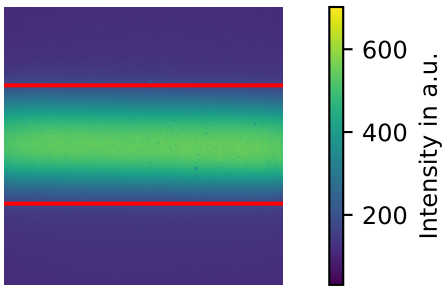

Figure 23: Fiducial cut in red, the requirement for the pixel intensity is set at the upper 99 percentile of the background distribution and the requirement for a row to survive the selection was that at least 90% of the pixel exceed this threshold.

A remaining challenge lies in fiducialising the data in the z-direction. This should determine when the light sheet is inside the crystal. Given the lack of clear indicators where the laser light meets the crystal surface, combined with the influence of surface effects (like the illumination of dust), another method is needed. One approach involves using the intensity difference of consecutive planes. This differ-

[6] *non-illuminated* region in Fig. 21

ence is squared, such that one can neglect the sign. We select the region where this value is below a threshold. This value is determined using the n^{th}-percentile of the distribution from the squared derivatives, where n is calculated by dividing the number of illuminated planes by the total number of planes. The number of illuminated planes can be roughly estimated, since we start the scanning procedure around 50 μm before the crystal surface. This strategy might not be the most precise in determining the exact location of the crystal, however we obtain a data set with a stable average intensity, which means that surface effects are reduced. The result for a scan of the *100 kRad* sample can be seen in Fig. 24.

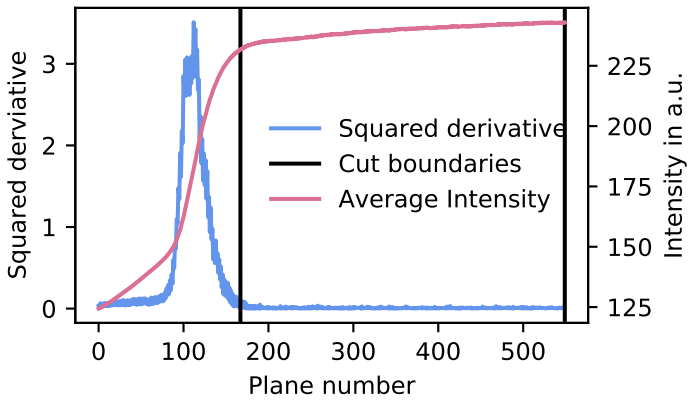

Figure 24: Fiducial cut in the z-direction, with the average intensity in blue and the squared differences between consecutive planes in red. The black lines indicate the selection.

Upgraded mesoSPIM

The data shown in Fig. 23 and Fig. 24 was acquired with the standard mesoSPIM and exhibits a distinctive illumination profile compared to data captured with the upgraded version. Two key features of the upgraded mesoSPIM are uniform illumination within the set galvo amplitude and the clear visibility of the edges of the illumination. The latter can be seen in Fig. 25 and calls for a reconsideration of the fiducialisation methods.

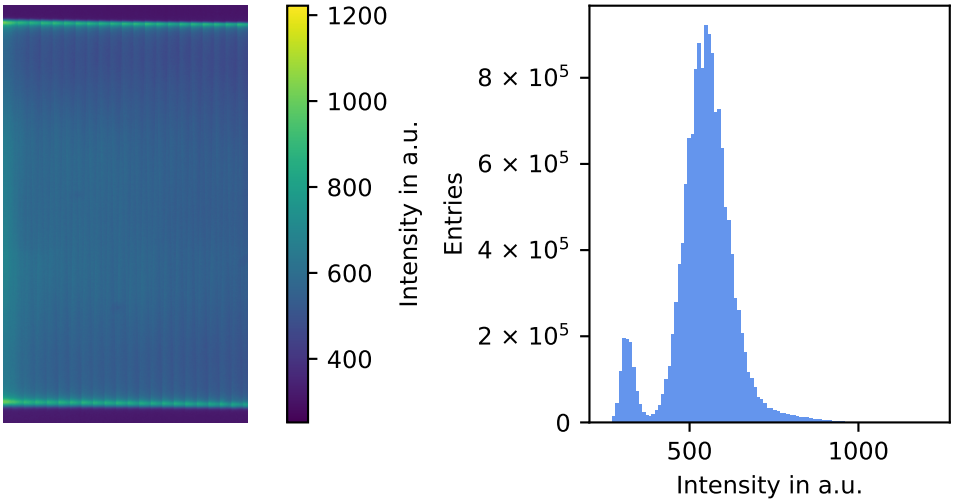

Figure 25: Example plane (left) including corresponding intensity profile (right). The illuminated region is larger in comparison to Fig. 21. In addition, the illumination boundary is very bright.

Again we start with the x-y-fiducialisation. In contrast to the standard mesoSPIM, the upgraded version produces data where the boundaries of illumination are more apparent. Therefore, we do not have to find them like we did in the data sets from the standard mesoSPIM, but we need to find a method of detecting the illumination edges. In addition, these boundaries are very bright, such that it would lead to a bias, for example in the pixel matching which will be discussed in section 5.3. Hence, these regions of high fluorescence need to be excluded. This is done by estimating the distribution of the illuminated pixel and defining an upper threshold. If the average of a row or column exceeds this threshold it is not considered for the fiducial volume. We define the fiducial volume as the largest region of neighboring rows and columns where the average is below this threshold.

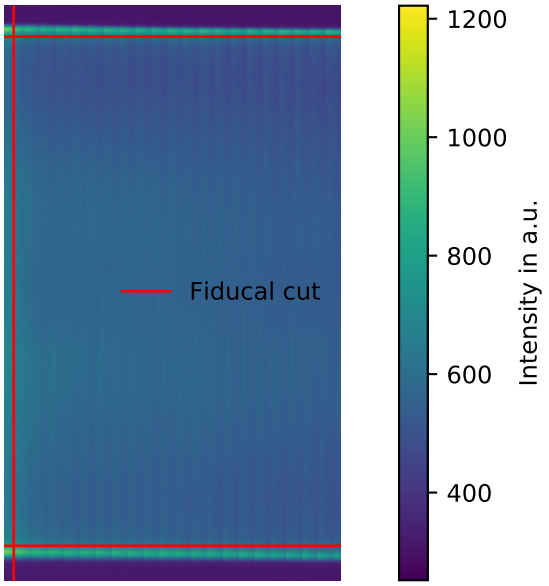

Figure 26: This figure shows the fiducialisation in the x-y-plane. The region of interest is not only restricted in the vertical direction but also in the horizontal one. This is due to the fact that the pixel on the left side also posses a higher intensity.

Regarding the fiducial selection in the z-direction, the same method as for the standard mesoSPIM can be applied, although defining the threshold is not straightforward. The intensity fluctuations from plane to plane are much higher, affecting the derivatives. Another possible method involves the use of normalized cross correlation, which is a technique for identifying characteristic features (see Appendix B), to compare each plane to the subsequent one, selecting the largest consecutive region above a given threshold. The advantage of this method is that it should be possible to apply the same threshold for all the scans, because it is not dependent on the absolute intensity of the pixels and the ratio of illuminated to non-illuminated pixels. The drawback is that without clear features of the scan, such as the high-intensity illumination edges, this method can not be applied and is therefore less relevant for the data taken with the standard mesoSPIM. The result can be seen in Fig. 27.

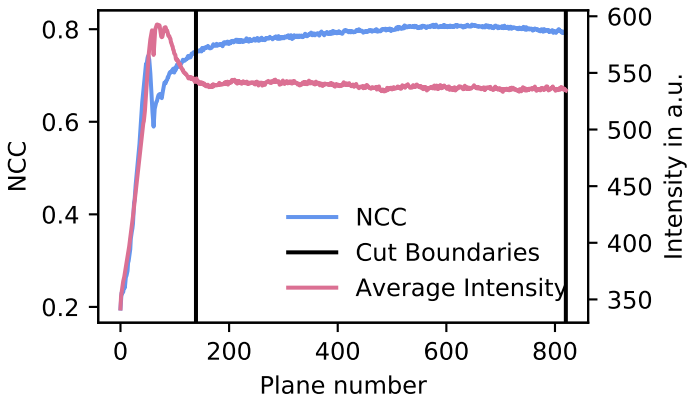

Figure 27: Fiducialisation in z-direction with the normalized cross correlation (NCC) between consecutive planes and a corresponding threshold of 0.75.

In conclusion, this chapter presented different methods of fiducialising data. A data-driven approach was used, aimed at achieving a highly homogeneous dataset, where illumination and overall intensity levels are comparable. These methods can be used for highly irradiated samples to determine the fiducialisation for non-irradiated samples with the same mesoSPIM settings. This is showcased in Fig. 28, where the fiducialisation has been determined with the *100 kRad* sample and applied to the *blank* sample.

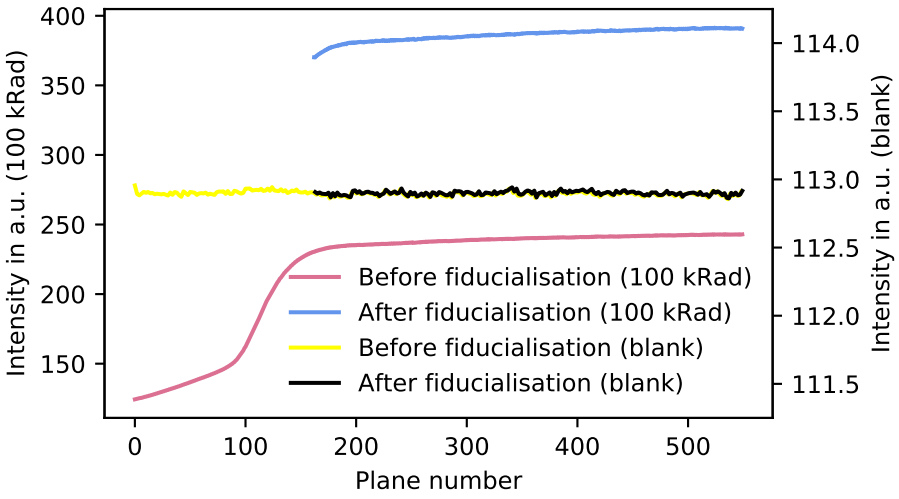

Figure 28: Comparison of the effect of the fiducialisation between the *100 kRad* and *blank* sample. The mesoSPIM settings were identical for both scans. The effect of selecting the illuminated region on the average pixel intensity per z-plan is visible for the *100 kRad* sample. In contrast, this effect can not be seen for *blank* sample.

5.2 Track Finding and Matching

Although we do not expect neutrino- or DM-nucleus scatterings to form elongated tracks of color centers spanning several micrometers, understanding the process of color center formation could be facilitated by examining fluorescent structures inside the crystal. In this chapter, we explore tracks measured by the upgraded mesoSPIM and provide an algorithm employed to identify existing track-like structures and designed to aid in future track discoveries. Furthermore, the track structures are compared with those from a repeated scan to further validate their existence and test the reliability of the scanning procedure. Below, we outline the key components and methodologies that will be addressed in this section:

- **Track Finding Algorithm:** The track finding algorithm aims to find elongated high-intensity structures in the dataset.
- **Parameter Testing:** There are three adjustable parameters in the algorithm: Kernel-size, threshold and density requirement. These will be tested to exclude the discovery of random high-intensity pixel structures.
- **Track Matching:** We will compare found structures to a repeated scan and thereby quantify the degree of similarity between the original structure and the one in the repeated scan.

After highlighting the components and methodologies, it is important to understand the sequence in which the data is processed. Below are the steps detailing how this data processing unfolds:

1. The dataset is fiducialised in the z-direction, such that we end up with the illuminated planes inside the crystal.
2. We fiducialise in the xy-plane to remove the non-illuminated regions, as well as the high-intensity illumination edges.
3. Then we apply the track finding algorithm, which searches for high-intensity structures inside the dataset.
4. This is followed by the track matching method, where we compare the found structures to a repeated scan, to verify their existence.

Track Finding Algorithm

Within the context of this work, we classifiy tracks as dense formations of color centers, hence visible as high-intensity pixel structures. Initial observations of these tracks were made by eye in a dataset acquired with the upgraded mesoSPIM utilizing ten times optical zoom on the *100 kRad* sample. This observation led to the idea of developing a technique to discover more structures. Although there are several possibilities to detect structures like Density-Based Spatial Clustering of Applications with Noise (DBSCAN) [49] or K-means [50], these turned out to not be particularly effective in handling large data sets nor optimized for use on a scan where the values are given in form of pixel intensities in the rows and columns of the two dimensional plane. Therefore, we implemented a custom method tailored to our dataset.

This new approach, referred to as the track-finding-algorithm, utilizes a combination of normalizing, thresholding, and array convolution to identify the structures. The need for normalization becomes evident as we recall from the previous chapter that the average pixel intensity varies from plane to plane during the scanning process.

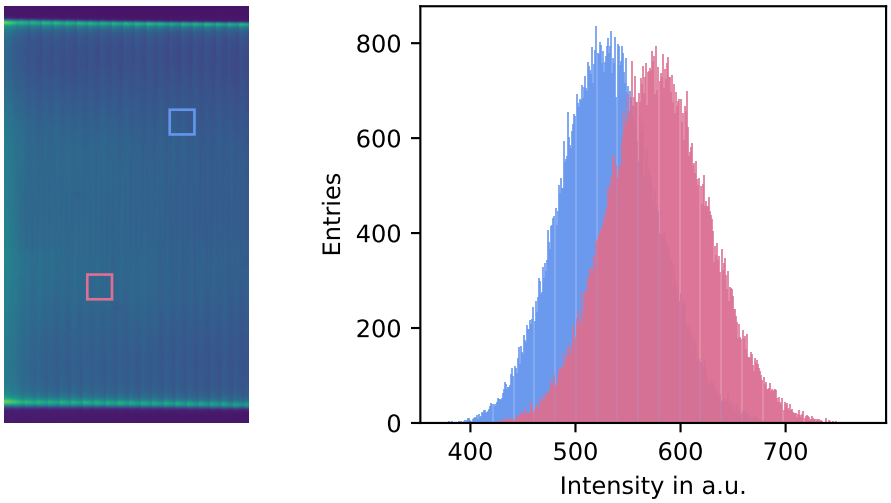

Figure 29: Comparison of the intensity distribution of two smaller regions in the same plane.

Furthermore, a single plane is also not homogeneously illuminated, which means that different regions have a slightly different pixel intensity distribution, as illustrated in Fig. 29. This difference would lead to a bias which has to be removed. To achieve this, the plane is divided into smaller segments (see Fig. 30), each analyzed separately. A single segment can be seen in Fig. 31.

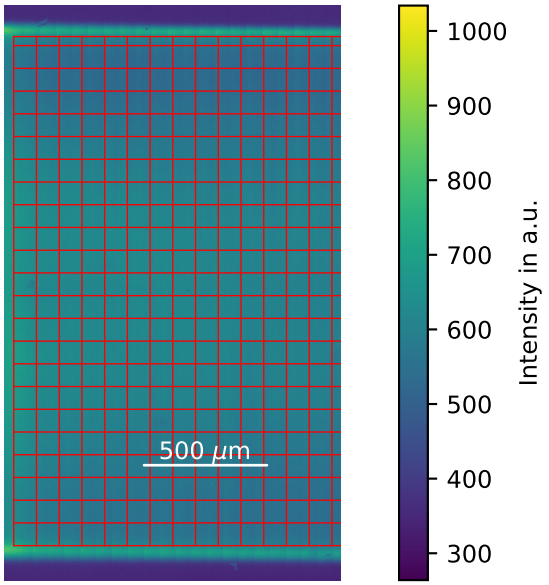

Figure 30: Segmented fiducial volume, where every region will be analyzed individually to find high-intensity structures.

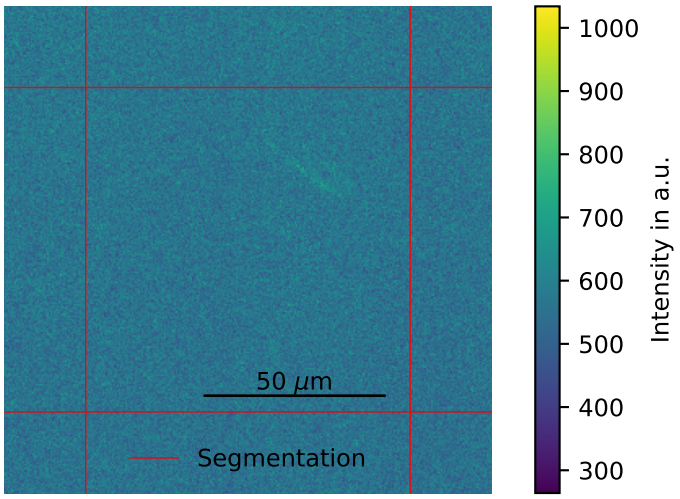

Figure 31: Single segment where a structure can be seen by eye in the top right corner of the segment.

These segments are normalized first, enabling the use of the same threshold universally. The next step involves applying the threshold, leaving only the pixels with an intensity above this threshold. The pixels surpassing the threshold, as seen in Fig. 32, are then overlaid with a two-dimensional array to form connections with other high-intensity pixels. This procedure is often referred to as convolution with a kernel in image processing terms [51]. This leads to the formation of connected regions where another threshold is implemented to filter densely populated structures and discard findings caused by random intensity fluctuations. The result for the example in this section can be seen in Fig. 33.

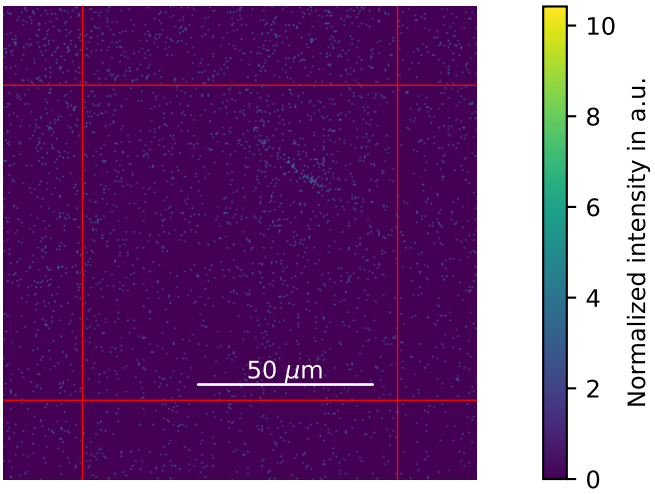

Figure 32: Normalized segment with applied threshold, such that only high-intensity pixel remain. By looking closely we can identify a dense region of pixels with an intensity above the applied threshold in the top right corner inside the segment.

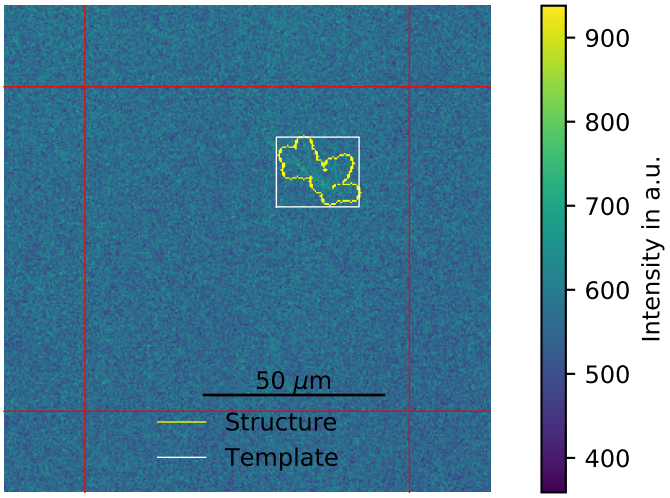

Figure 33: Outline of the identified structure in yellow, enclosing the high-intensity pixels. The white box (also referred to as template in the following sections) will become important when we compare the found structures to repeated scans.

Parameter Testing

The process of track identification uses several parameters to search and connect high-intensity pixels: threshold, density requirement and kernel-size. The likelihood of discovering a structure depends on the interplay of these parameters, which makes a simultaneous optimization necessary. The two goals of this optimization are to prevent false positives, which are random structures being misidentified as tracks, and ensure all genuine structures are correctly recognized. The first aspect can be assessed by creating test datasets without any structures and verifying how many false positives emerge. The second aspect is more complicated as it requires knowledge of the number of tracks, or would need an extensive manual process of labelling each structure as random or genuine. This section focuses on parameter testing with an aim to avoid classifying random features as tracks.

We can test the parameters for random feature detection by using different parameter pairings in the track finding algorithm and apply it to a randomly generated dataset. Since we normalise the pixel intensity after the segmentation, we are tempted to generate a random dataset by sampling the pixel intensity from a Gaussian distribution centered at 0 with standard deviation of 1. However, the actual dataset can exhibit a significant amount of outliers, altering the shape of

the distribution, which is not perfectly gaussian as a result. Therefore, the data is shuffled to yield the desired random distribution. The parameters are then tested by repeatedly running the track-finding algorithm over the dataset, each time shuffling the pixels within the segments. The structures discovered in these tests are then counted and summarized in figures such as Fig. 34.

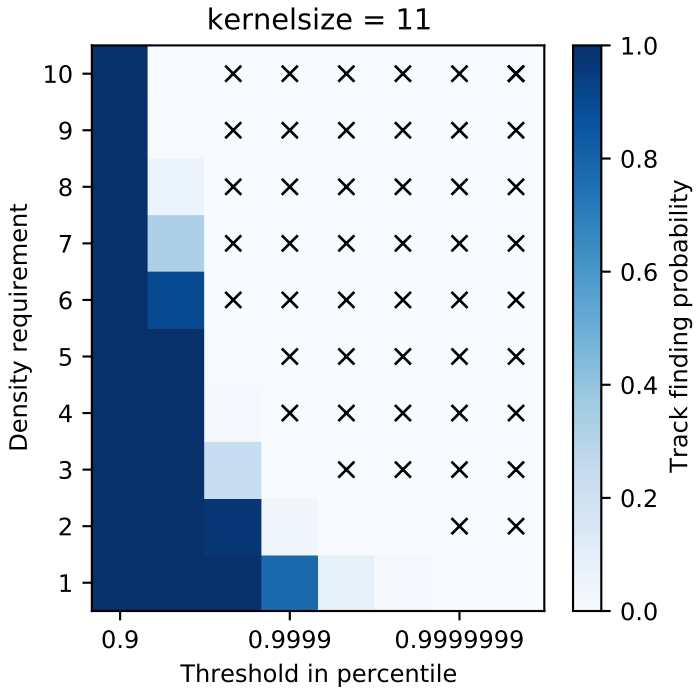

Figure 34: Probability of finding a random structure with the given parameters. Here the fixed parameter is the kernel-size, which is the search radius to connect high-intensity pixels. In addition, the probability depends on the threshold and density requirement. The crosses mark the parameter pairings for which the probability was zero in a simulation, where a single plane was sampled 5000 times.

If the threshold and density requirement is low, numerous structures are identified. Intuitively, the number of found structures also increases with larger kernel-sizes. These results allow for the selection of parameters that should eliminate false positive discoveries. However, this approach provides no information on the effectiveness of identifying genuine structures, a topic we will delve into in the following section.

Track Matching

With optimized parameters, the likelihood of false positives due to pixel intensity fluctuations should be minimized. However, features in the microscopy data due to other microscopy effects might still be present. To avoid misidentifying these features, we can compare the tracks with those from a repeated scan, obtaining insights into the performance and consistency of the microscopy procedure itself. Considering the track-like example from the previous section, the structure is visible in both scans shown in Fig. 35 and our goal is to further quantify the certainty of its presence and features. For this purpose, the *match_template* [52] tool from the *skimage.feature* library comes in handy. This module facilitates image comparison to evaluate the level of matching. This method can also be used to compare a small section of an image with all similarly sized sections of another image. Therefore, we will use it here as a tool to evaluate the matching of structures in repeated scans.

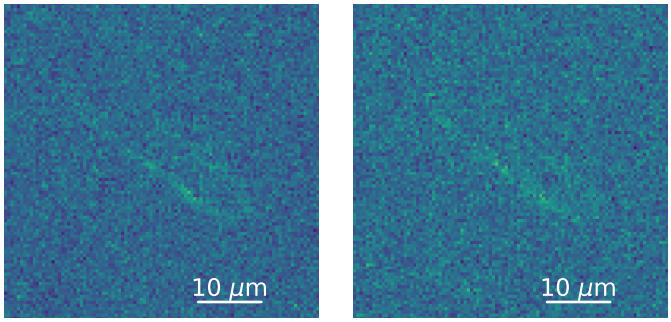

Figure 35: The structure found in a dataset of the *100 kRad* sample on the left. On the right is the same region from a repeated scan where the structure can be observed as well.

When a structure is identified, the rectangular area enclosing it is extracted and used as a template (see Fig. 33). This template is then compared via the normalized cross correlation (NCC) to all possible spots on the plane. The resulting NCC values range between -1 and 1, where 1 indicates a perfect match, -1 an anti-correlated match, and 0 denotes the mean of a random distribution. The distribution of these values for all the potential spots yields a Gaussian-like distribution centered around 0, with the standard deviation dependent on the size and shape of the template and the enclosed structure. The NCC distribution for the previous example is displayed

in Fig. 36.

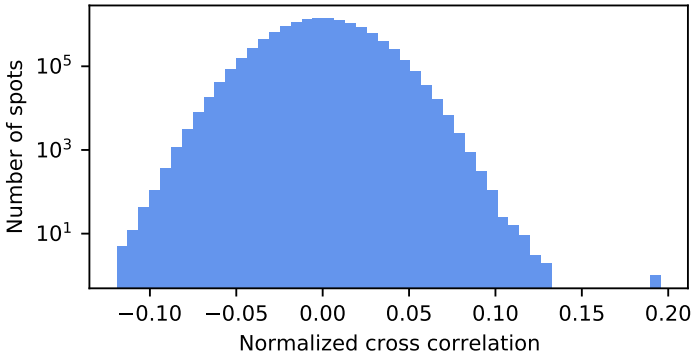

Figure 36: Normalized cross correlation values for all the possible locations where the structure from Fig. 33 was compared to. This value will be normalized to compare to other NCCs from other tracks, here however it was left as observed to display the values in the range from -1 to 1. The value is relatively low for the best matching location (sole point to the right), considering a perfect match at 1. This can be explained by the random pixels surrounding the structure which are also part of the comparison. Nevertheless the benefit of the NCC reveals itself by considering the total distribution and realising that this value is 8.8 sigmas away from the mean.

To facilitate the comparison of different structures, the NCCs are normalized to yield a Gaussian distribution centered around 0 with a width of 1. These transformed values are referred to as *adjusted NCC*. With this normalization the standard deviation of any comparison can be directly observed. Subsequently, a threshold is established above which an NCC value is considered a match. An example threshold can be set at 6 sigma, where the chances of having a random match above this value is close to 10^{-9}.

Examples

In this section, we examine high-intensity structures and compare them with those from a repeated scan. These examples, discovered using the track-identification-algorithm, were found in the *100 kRad* sample. The data was collected using the upgraded mesoSPIM with 10 × zoom.

In the first example (see Fig. 37) the track-finding method indicates a discovery of a structure. When applying the track matching method, we observe that the

structure does not fully match features in a repeated scan. The random pixel intensity fluctuation from several pixels could have lead to the 'discovery' of this structure in the first place, but the low correlation value obtained from the track matching (bottom of Fig. 37) rather indicates that this feature, initially assigned as a potential track, has a random origin.

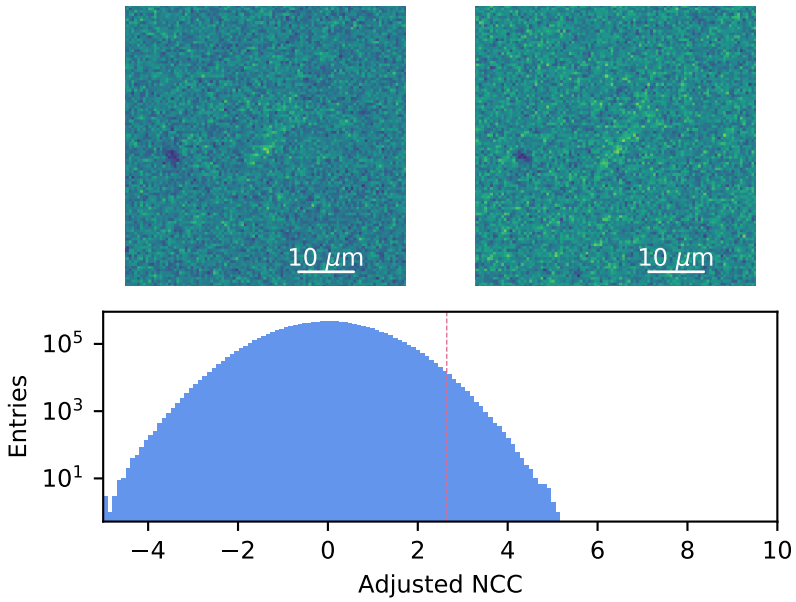

Figure 37: On the top the same sections from two different scans containing a high intensity pixel structure are shown. On the bottom we see the normalized cross correlation coefficient, which compares the the structure from the left to all possible regions in the z-plane from the scan which contains the structure shown on the right. Here the structures do not match very well and they are thus not considered genuine structures. The red line marks the correlation values of the structures.

In the second example (Fig. 38) we observe a high NCC for the matching of the structures. In both cases a high-intensity region is present, which is roughly 5 μm in size, followed by a tail going towards the top left corner of the pictures, consisting of less intense pixels. We can only speculate about the origin of this structure, but such 'tracks' are probably not created by photons and must therefore have another origin.

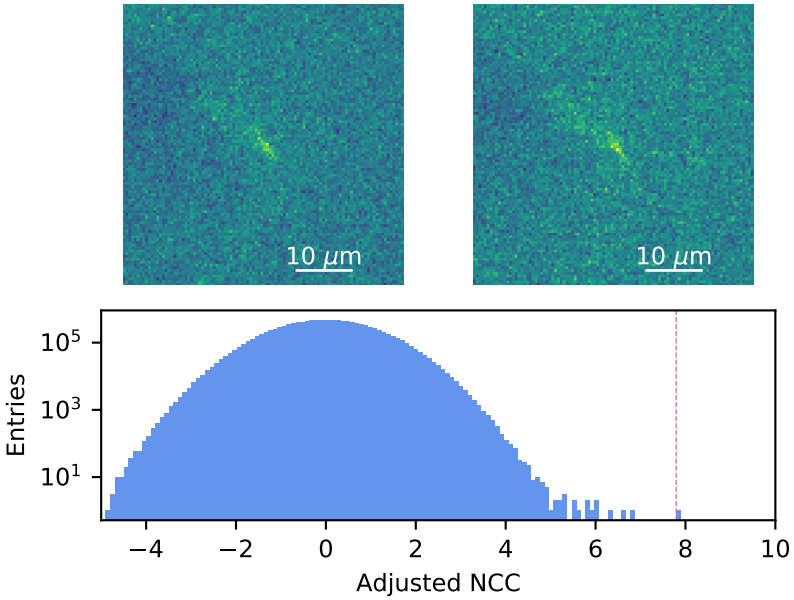

Figure 38: This example shows a very well matching structure, which is also reaffirmed by the NCC, displaying a standard deviation of nearly eight sigmas to the assumption to random matching, which is displayed by the red line in the figure on the bottom. This line marks the comparison at the same coordinates in the repeated scan.

Analysis Outlook

The success of the track-finding algorithm lead to the idea of irradiating additional crystals. The goal of this is to create tracks which are longer than 40 μm by irradiating the crystals either with protons or alphas. In addition, different materials should have been irradiated to observe and study the response of the compound and get insights on the formation of color centers.

We were in contact with the Laboratory of Ion Beam Physics Zurich (LIP) which is part of the ETH and located at Hoenggerberg. The samples would have been irradiated with 3 MeV protons and perhaps 5 MeV alphas. The advantage of the protons is that they produce longer tracks, however the density is expected to be low, since only about 1% of the energy goes into nuclear recoil [53]. On the other hand, alphas would deploy more energy into nuclear recoil, but the length of the track would only be around 10 to 20 μm.

Once the irradiation settings were determined, it was time to search for suitable

materials. The requirements are summarized in the following. The irradiation should lead to tracks longer then 40 μm, the formed color centers should have emission and absorption spectra in the range of visible light and lastly the crystal should not become radioactive. As part of this work the track length was estimated using simulations with the TRIM simulation package [54].

A material candidate is CaF_2 which has been studied extensively throughout this project and is expected to form tracks in the range of 50 μm. Another candidate is LiF, where longer tracks could be induced (around 73 μm in response to 3 MeV protons). The drawback here is that the F-centers do not fulfill the requirement of the spectra, but the F_2- and F_3^+-centers do [55]. Therefore we need to have adjacent F-centers for a successful detection. The last candidate is sapphire (Al_2O_3), where the track length is expected to be around 50 μm. The emission peak of the F-center is at 410 nm, which is in the visible range, unfortunately the absorption maximum is at 210 nm and therefore in the UV spectrum. However, there is a non-zero contribution also from visible light, which suggests that it could be possible to trigger the PL [56].

Unfortunately, the irradiation of these samples was laid off due to maintenance of the ion accelerator. Therefore, the analysis of structures came to a hold. The data from these samples would have been used to study the track and color center formation in the crystals. This would have helped to validate the track-finding algorithm and, if successful, to further optimize the parameters, in terms of how well structures can be identified.

5.3 Pixel Matching

Building upon the work completed in the previous section, where high-intensity structures were identified and compared, this chapter seeks to extend this process by focusing on individual pixel matching. Given that neutrinos and dark matter are expected to often produce only a single color center, identifying single high-intensity pixels is critical. In the following we will detail the strategy to determine the number of matching high-intensity pixels. For this work, we use data from the *100 kRad* sample. This section is structured in three parts:

- **Reduce systematic effects:** We need to identify and reduce systematic effects, which could lead to wrong estimations of the number of high intensity pixels in the same position which are attributed to the existence of color centers.
- **Estimate random matching:** The pixel intensity can fluctuate, which causes random matches. By estimating the amount of random matches, we can determine an excess of genuine matches in the data.
- **Matches in data:** In the last part, we concentrate on the matches within the data. Using our developed methods, we identify the surplus of matches found over the expectations by random chance.

Systematic Effects

Systematic effects that degrade data quality can arise from various sources, including non-homogeneous illumination, pixel malfunctions, and optical path pollution, such as dust on the crystal or lens. Each of these factors can affect the observed pixel intensity.

Non-homogeneous illumination is a recognized limitation of the mesoSPIM. Like the track-finding algorithm, we can use segmentation followed by normalization of the fiducial volume to minimize this effect. However, because we are now dealing with single pixels, slight changes in intensity can have a significant impact. Hence, the relationship between pixel matching and segmentation size needs to be carefully

evaluated.

Malfunctioning pixels, which do not accurately represent the condition of the crystal, pose another problem. They can either display a consistently high-intensity throughout the scan or fail to respond to light from fluorescence. We prioritize removing the former as they could lead to false positives, while non-responsive pixels do not affect the detection of matching pixels but should be considered when adjusting statistical analyses.

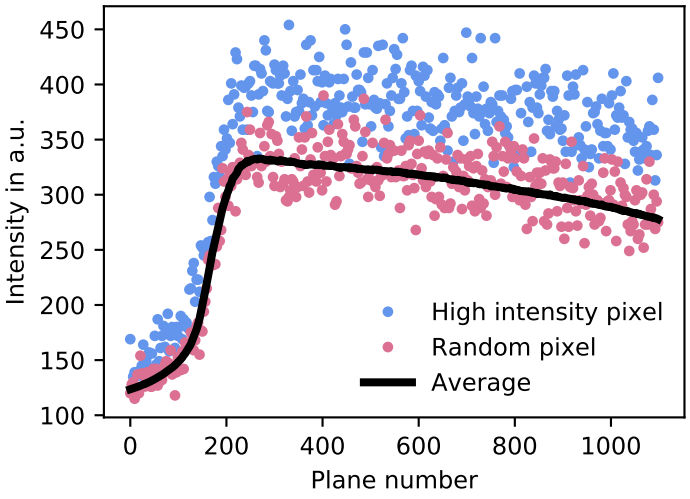

Figure 39: This figure displays the intensity distribution for two individual pixels, shown in blue and the average intensity per plane in red. The xy-coordinate of the blue pixel is excluded due to its consistently high-intensity throughout the scan.

We remove always-bright pixels by ensuring the median pixel intensity is no more than one standard deviation away from the mean intensity. Non-responsive pixels, which do not influence the detection of matching pixels, are left in the data.

The last of the three mentioned systematic effects is the pixel intensity decrease due to pollution in the light path. An example for this effect is observed in Fig. 18. Similar to the pixel which do not respond to illumination, these pixels do not lead to false positives and can be neglected for the moment.

Random Matching

Pixel matching involves finding high-intensity pixels at the same position across multiple scans. However, pixel intensities can fluctuate, leading to random matches. Hence, it is crucial to estimate random matches to identify any excess, which indicates that it is possible to match pixels and thereby identify color centers.

The procedure for estimating random matches is similar to that of random structure testing. In this case it involves only two parameters: the segmentation size and the threshold. After these parameters are selected, the fiducial volume is compared to two repeated scans segment by segment. The pixels in each segment are shuffled to create randomness. If a pixel in all three scans exceeds the threshold at the same spot, it is considered a match. In Fig. 40 we see the expected random matches using a normalization window of 100 × 100 pixels. In addition, the matching percentage is displayed, which is calculated by dividing the total matched by the number of pixels above this threshold. The observed decline is in correspondence with the expectation from random matching.

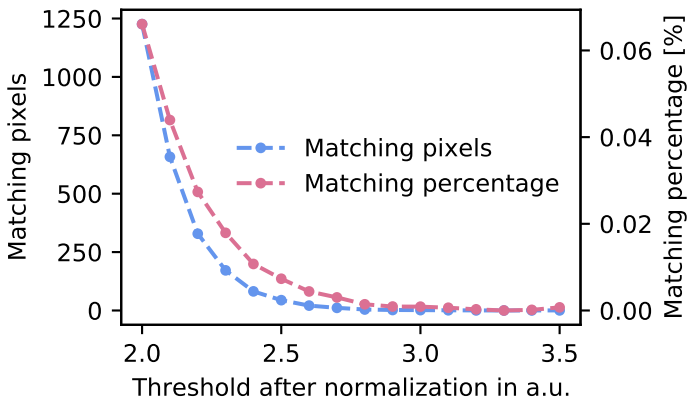

Figure 40: This figure shows the average number of random matches found in 10 runs (shown in red), and the percentage of matched pixels (blue) which exceed the set threshold.

Matches in Sample Data

This section will analyze the number of matching pixels in the *100 kRad* sample, taking into account the selected threshold and segmentation size. The irradia-

tion with gammas led to high PL and therefore also a high number of matches is expected. We will then compare these numbers with the random matching estimations to determine if there is an excess.

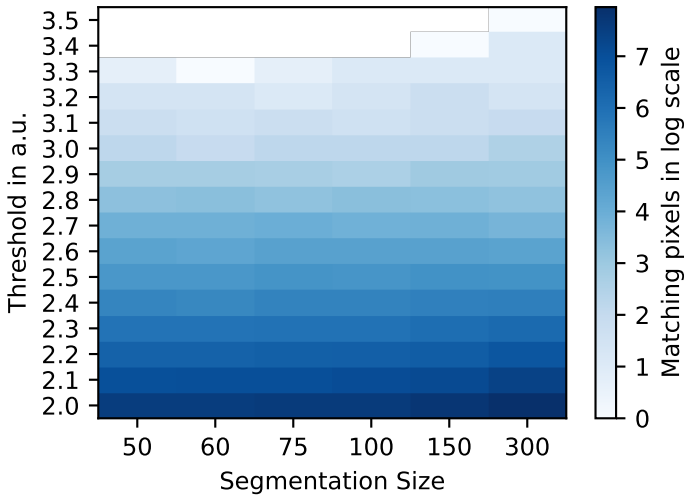

Figure 41: This overview of pixel matching in the real data displays the log-scaled number of matches in relation to the threshold and segmentation size. There are slight differences. For example the large segmentation produces more matching pixels, this is an effect of the inhomogeneous illumination and the resulting regions with higher intensities.

Given the bias introduced by larger segmentation sizes, we select a smaller segmentation size. Fig. 42 compares the number of matching pixels for three smaller sizes. As the number of matching pixels converge, the 50 $\times$ 50 segmentation size is chosen for further analysis.

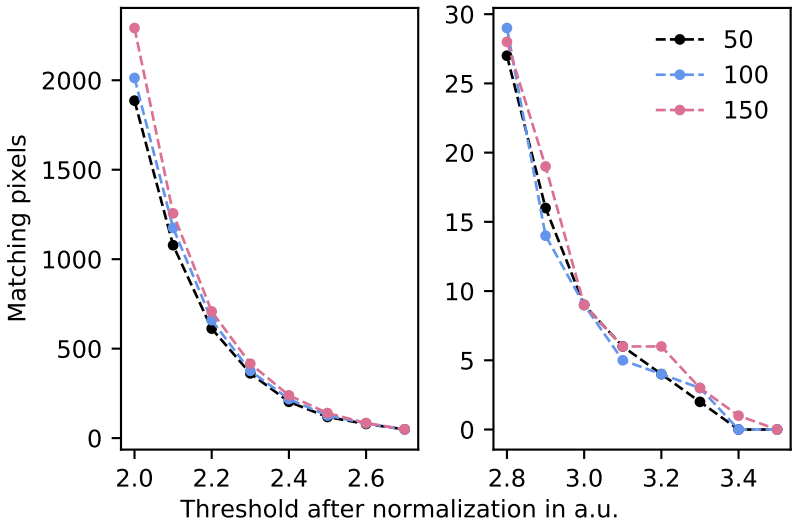

Figure 42: This plot shows the number of matching pixels in the data in relation to the applied threshold after normalization for different segmentation sizes. The segmentation is achieved through squares, their respective side lengths are denoted in the legend .

Having fixed the segmentation size, we can compare the discovered matches to the number of random matches. Fig. 43 displays the found matches in relation to the threshold. A clear excess of matches is observed in the data. This suggests that the brighter spots have a physical reason and the matches are not formed by coincidence.

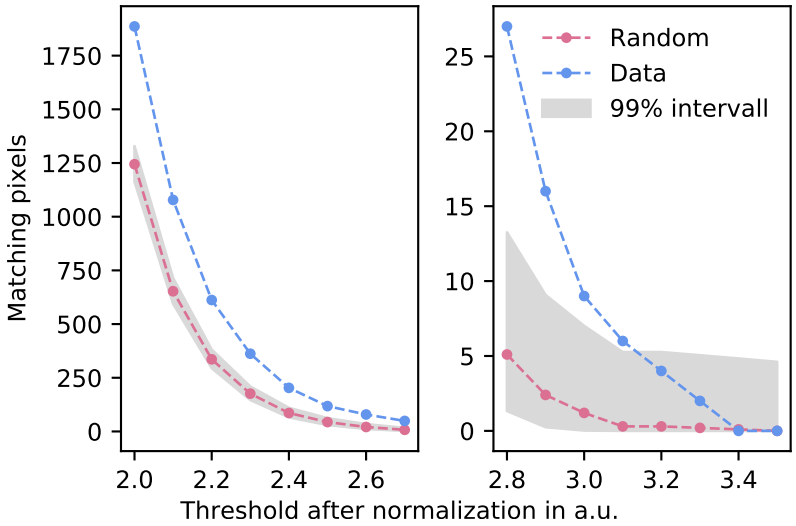

Figure 43: Comparison of the number of matching pixels (blue) to the expectation from random matching (red) with the 99% confidence interval in grey. At low thresholds, the excess is large and reduces at higher thresholds.

This section concludes with an examination of an example from a matching pixel and shows how the intensity evolves for the same xy-coordinates across several planes (see Fig. 44). This figure illustrates the need for the comparison of several repeated scans, since in plane 382 two of the three scans would indicate a match at these coordinates, while the third gives reason to doubt the existence of a genuine match by displaying a rather low intensity. Mathematically the probability of random match occurrence reduces from 1.8×10^{-6} to 2.5×10^{-9} if we consider high intensity pixels, which have an intensity of at least 3 standard deviations above the mean.

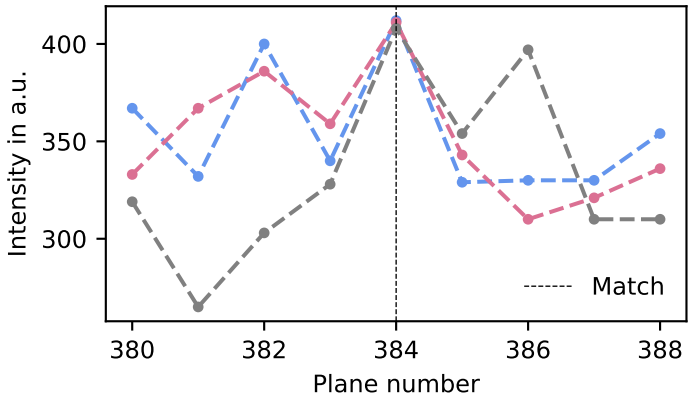

Figure 44: Here we see the intensity of three pixels from repeated scans across nine planes. In plane 384 we observe a match.

5.4 Neutron Irradiated CaF_2

In this section, the neutron irradiated sample *VT303* will be analyzed. This demonstrates the use of the two methods discussed above for a sample where the PL was formed by nuclear recoil, which corresponds to the color center formation mechanism in DM and CEνNS searches. The analysis will include finding and matching structures and observing if there is a clear signal for matching pixels. This sample was irradiated with an AmBe source for about 29 hours with an estimated nominal dose of 6.6 $\times$ 10^7 n/cm^2. The scan was taken with the standard mesoSPIM. The crystal was illuminated using a 405 nm laser and recorded using a 6.3 $\times$ zoom in combination with the quad-filter, which filters out the following wavelengths: 405 nm, 488 nm, 561 nm and 640 nm. This should ensure that the scattered light is excluded from the observed signal, the expected wavelength is slightly larger than the excitation wavelength, this can be seen in [46]. There are 1749 planes in total, each with 2048 $\times$ 2048 pixels. The stepsize between individual planes was set to 6 μm and the image pixel size is 1.03 μm.

Structures

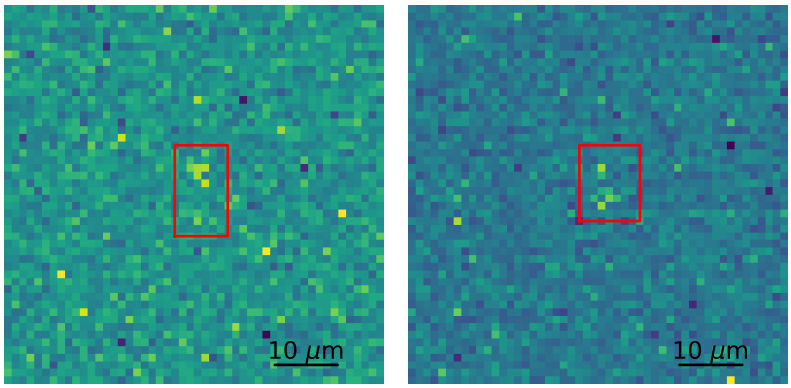

Figure 45: Examples of two structures found inside the neutron irradiated CaF_2 sample. Due to the larger pixel size the resolution is decreased and there is a higher dependency on the intensity fluctuations from individual pixels. This will impact the effectiveness of the track-finding algorithm.

Due to the larger size of individual pixels, the structures are expected to be constituted of fewer pixels than those shown in section 5.2. Therefore, the parameters have to be slightly adjusted. In addition, neutrons are not expected to form color

center tracks, which means that observed structures are most likely caused by pre-existing defects or cosmic rays.

The track-finding-algorithm finds 107 structures, examples can be seen in Fig. 45. Visually, they do not exhibit a clear structure as seen previously. This observation is backed up by the distribution of the normalized NCCs in Fig. 46, which are computed by comparing the templates (see Fig. 33) with the repeated scan at the same coordinates. Only two structures display a NCC value which deviates 5 sigmas or more from the mean. These values were extracted in the same way as in section 5.2.

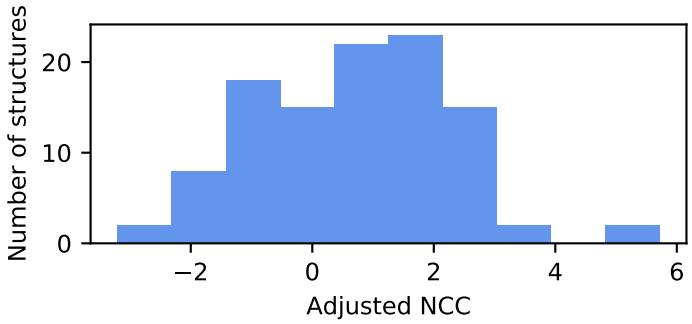

Figure 46: Distribution of the adjusted NCCs of the found structures compared with the repeated scan at the same coordinates. Most of these do not display a clear match, and are most likely not genuine structures.

The best matching structure can be seen in Fig. 47 with the comparison of the repeated scan. While one pixel consistently appears with high-intensity in the repeated scan, the surrounding pixels appear random, making it challenging to identify the entire formation as a genuine high-intensity structure.

The absence of recurring structures may result from two factors. First, the pixel size in this scan is notably larger than that in section 5.2, being 1.03 μm compared to 0.425 μm. This disparity means fewer pixels are resultant from a structure of the same size, which makes the detection and matching more dependent on intensity fluctuations. Second, irradiation with neutrons was not expected to produce large structures. Albeit a single color center may yield several pixels lighting up given the point spread function distribution.

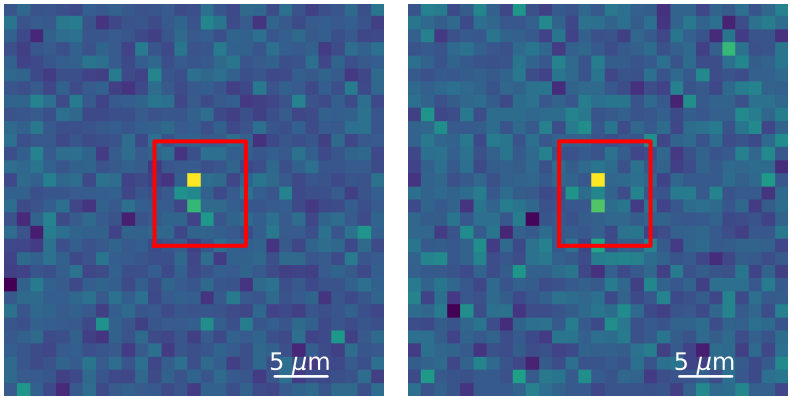

Figure 47: Comparison of the structure with the highest matching coefficient to the pixels in the same location of the repeated scan. The bright pixel (yellow) is present in both scans, while the other intensities seem to fluctuate.

The high number of detected structures, even though they do not have a high matching coefficient in the repeated scan, make it worth to check if there is a bias in the algorithm. This bias might arise from the illumination, which would reveal itself if numerous structures are found in close proximity based on their x-y-coordinates. Additionally, it could be that the segmentation leads to a bias which will also be investigated.

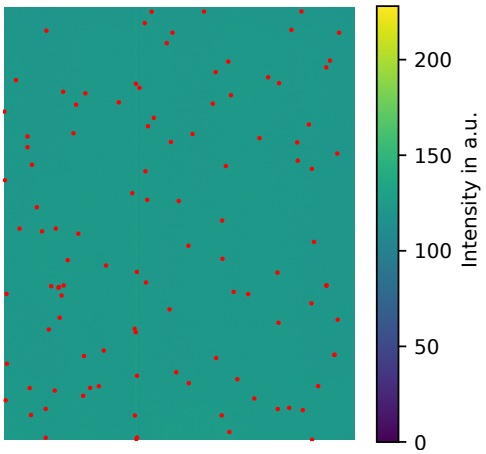

Figure 48: Distribution of the structures projected onto a single plane (1738 × 1490 pixel). The pixel intensity values in this figure are only for illustration purposes.

We start with examining the distribution bias in the plane. For this purpose all structure centers are projected to the front, see Fig. 48. A χ^2-test reveals that

neither the distribution in x-, y- nor z-direction are statistically incompatible with the hypothesis of a uniform distribution.

The final test is to determine if the structures are also uniformly distributed with respect to the segment. As a reminder this segmentation was used to remove a possible bias from the non-homogeneous illumination. As shown in figure Fig. 49 the segmentation does not lead to a bias, which was also verified by using a χ^2-test.

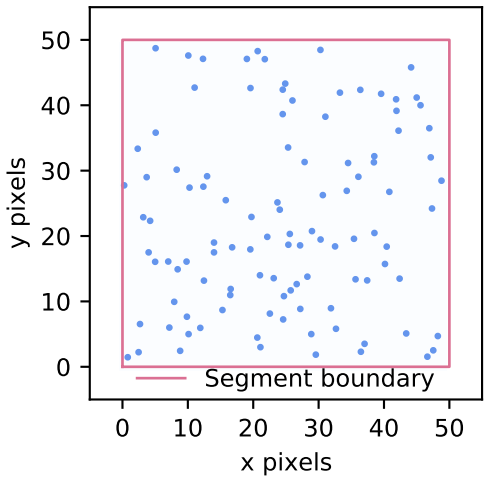

Figure 49: Overlay of the 50×50 pixel segments to search for biases inside the individual search regions. No region was particularly favored by the track-finding-algorithm.

Pixel Matching

The irradiation with neutrons should lead to color centers, and therefore also fluorescing pixels. These pixels will be matched with three repeated scans. The exclusion of pixels which constantly show a high-intensity and the segmentation as described in section 5.3 will help to make an unbiased estimation of the matching pixels.

In a first step the number of matching pixels will be compared to the estimated random matching number. This will be done in relation to the applied threshold after normalization. The results can be seen in Fig. 50.

The count of matching pixels in the data exceeds what one would anticipate from random matching by a large margin. However it is important that potential biasing is excluded. There are tests that can shed light on the causes, especially if the effect is not caused by irradiation.

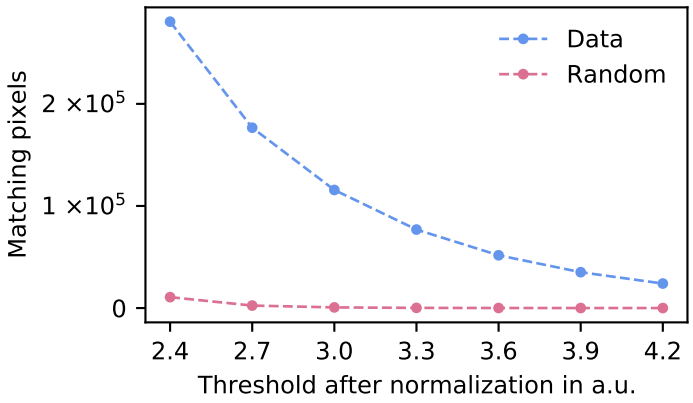

Figure 50: Number of matching pixel for neutron irradiated CaF_2 compared to random matching in relation to the applied threshold.

First, one can check the frequency of each individual pixel. This means counting how many times the same x-y-coordinates displays a match in different planes. This has to be compared to the expectation of randomly distributed matches, which is shown in Fig. 51.

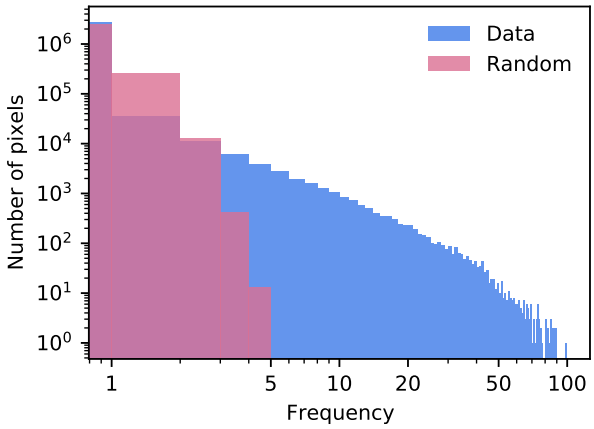

Figure 51: Histogram of the frequencies, which display the number of matching pixels at the same x-y-coordinate.

Given that each pixel should have an equal likelihood of matching the repeated scans, we can define an upper limit for the frequency. In the dataset used in this section, the upper limit is 5, which can be seen in Fig. 51. We consider a pixel to be noisy if its frequency surpasses this limit. For this purpose the number matches from the real data are randomly distributed several times, the maximal observed frequency in this simulation will be taken as an upper limit. This approach significantly reduces the number of matching pixels, as illustrated in Fig. 52.

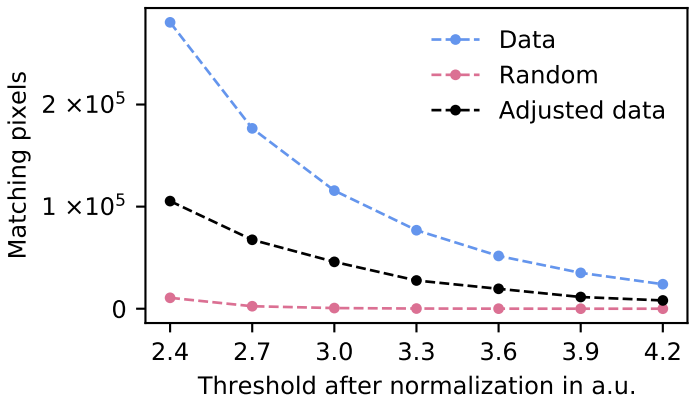

Figure 52: The pixels with an unusual high frequencies are removed, which leads to the adjusted number of matching pixels. We observe significant decrease in the number of matching pixels, but a large excess in comparison to random matching remains.

The next step in detecting potential bias involves analyzing the spatial distribution. The spatial distribution of the matched pixels can be studied in a projection to a single plane. This leads to the results in Fig. 53, which shows no sign of a spatial bias.

This statement is reinforced by Fig. 54, which shows that there is no favored region for matching pixels. In addition, a Wald-Wolfowitz [57] run-test was used to further investigate the dataset to observe hidden features. This confirmed that the points seem to be randomly distributed above and below the mean.

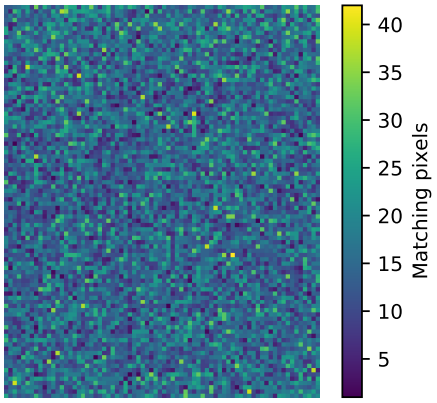

Figure 53: The figure illustrates the projection of matches onto a single plane. Multiple pixels are combined into patches to give a better overview over the number of matching pixels.

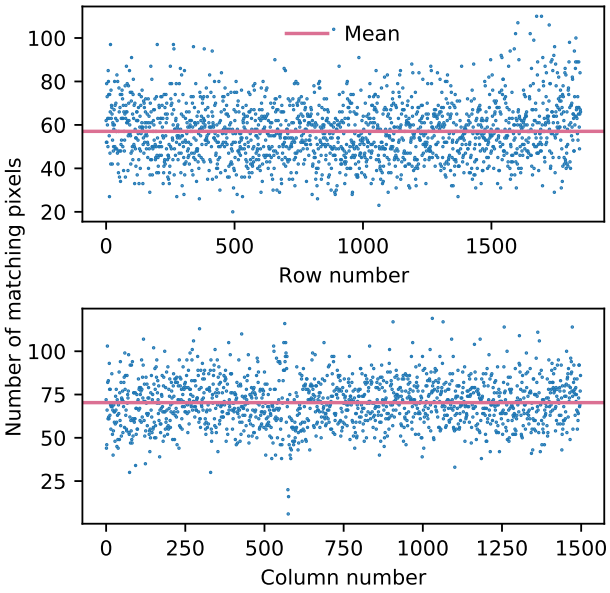

Figure 54: Number of matching pixels per row (top) and column (bottom) respectively, displaying random behavior.

In conclusion, the investigation of the neutron irradiated CaF_2 sample showed that there is a high number of noisy pixels, which was revealed by observing the high-intensity pixels matching frequencies in individual coordinates. In addition, we do not observe spatial biases in the distribution of matching high intensity pixels. Therefore, the excess of matching pixels in the scans of neutron irradiated samples in comparison to random matching strongly indicates that the matches are a result of the irradiation, which is a promising result for future studies.

6 Conclusions and Outlook

This thesis contains the starting point of the light sheet microscopy data analysis for PALEOCCENE. The PALEOCCENE approach uses passive crystals as targets for nuclear recoils, which can induce detectable color centers within these transparent materials. These lattice defects can be detected by light sheet microscopy. This technique illuminates and captures images of a thin section of a specimen, allowing for detailed three-dimensional imaging. As a result, the PALEOCCENE concept has potential for applications in the domains of Coherent Elastic Neutrino-Nucleus Scattering (CEνNS) and Dark Matter (DM) searches. In the first part of the analysis, a region of interest was defined within a CaF_2 crystal using fiducialisation methods, ensuring precise separation of illuminated regions from non-illuminated ones. In the second part of the analysis, we investigated track-like structures in the microscopy scans. While such structures are not expected outcomes of neutrino or DM-nucleus scatterings, we study these structures in order to understand color center formation. Within this context, a track-finding algorithm was developed that automatically identifies track-like structures. This algorithm considers tracks as dense clusters of high-intensity pixels. To ensure accuracy in the detection, we refined this algorithm to minimize the impact of false positives. Subsequently, rigorous validation was achieved through cross-correlation with repeated scans.
Additionally, we introduced the concept of pixel matching, which involved identifying high-intensity pixels consistently appearing across multiple scans. The capability to identify these features is essential because neutrinos and dark matter might produce only one color center. This procedure involves three major steps: reducing systematic effects, estimating random pixel matches, and analyzing matches in the actual sample data. Systematic effects, which include issues such as non-homogeneous illumination and malfunctioning pixels, were addressed to ensure accurate data readings. We encountered a noteworthy finding - an excess of matching pixels, far exceeding expectations from random occurrences, thus suggesting a physical origin for these brighter spots.
In the last chapter we applied the developed methods to the microscopy scans of a neutron irradiated CaF_2 sample. Our analysis revealed visually distinct structures compared to repeated scans, an observation validated through mathematical

cross-correlation tests. This indicated that these structures were, in fact, imaging artifacts rather than physical phenomena. In contrast, the count of matching pixels significantly exceeded the number of estimated random matches. Several tests were conducted to eliminate potential biases. Among these, frequent matching at specific x-y-coordinates was identified as noise and discarded, considerably reducing the match count. Yet, even after this adjustment, the match count remained significantly higher than the number that can be attributed to random matching. Spatial analysis did not indicate any discernible pattern or bias in the matching, reinforcing the idea that the matching pixels result from neutron irradiation.

The studies and analysis methods outlined in this thesis provide a robust foundation for future investigations within the PALEOCCENE framework using light sheet microscopy. Specifically the track finding and pixel matching methods can serve in the near future to find tracks from ion irradiation studies and derive a relation between neutron radiation dose and created color centers. These pioneering studies and analysis methods provide a solid basis for advancing our comprehension of color center formation and their visualization with light sheet microscopy, a fundamental aspect of the PALEOCCENE concept. The horizon of our research in this domain is expansive, inviting further exploration and discovery.

A Additional Figure Information

Additional information for the scans in the figures can be found in this spreadsheet [58]. Figures shown in this thesis correspond to the scan IDs as listed below.

Fig. 20 to Fig. 18 and Fig. 24 scan 41
Fig. 21 to Fig. 23 scan 22

Fig. 25 to Fig. 38 scans 69 & 70

Fig. 39 to Fig. 43 scans 47, 48 & 49

Fig. 45 to Fig. 54 scans 130, 135 & 140

B Normalized Cross Correlation

The cross correlation is commonly used in feature detection and is used in template matching as a distance measure as seen in Eq. 2. f is the image and t the template at position (u, v).

$$d^2_{f,t}(u,v) = \sum_{x,y}[f(x,y) - t(x-u, y-v)]^2 \tag{2}$$

This measure is not invariant under increase of the pixel intensity level and the range of d is dependent on the template size. Therefore one uses a normalized correlation coefficient as in Eq. 3 , with $\bar{f}_{u,v}$ being the mean of the region that is being compared and $\bar{t}$ the mean of the template.

$$\gamma(u,v) = \frac{\sum_{x,y}[f(x,y) - \bar{f}_{u,v}][t(x-u, y-v) - \bar{t}]}{\sqrt{\sum_{x,y}[f(x,y) - c]^2 \sum_{x,y}[t(x-u, y-v) - \bar{t}]^2}} \tag{3}$$

This results in a value in the range from -1 to 1, with 1 being a perfect match, -1 the anti correlated match and 0 indicating total randomness. More info can be found in [59].

References

[1]Particle Data Group et al., "Review of Particle Physics", en, Progress of Theoretical and Experimental Physics **2022**, 083C01 (2022).

[2]F. Zwicky, "Republication of: The redshift of extragalactic nebulae", en, General Relativity and Gravitation **41**, 207–224 (2009).

[3]V. C. Rubin and W. K. Ford Jr., "Rotation of the Andromeda Nebula from a Spectroscopic Survey of Emission Regions", The Astrophysical Journal **159**, 379 (1970).

[4]K. Freese, "Review of Observational Evidence for Dark Matter in the Universe and in upcoming searches for Dark Stars", EAS Publications Series **36**, 113–126 (2009).

[5]A. Arbey and F. Mahmoudi, "Dark matter and the early Universe: A review", en, Progress in Particle and Nuclear Physics **119**, 103865 (2021).

[6]L. Roszkowski, E. M. Sessolo, and S. Trojanowski, "WIMP dark matter candidates and searches—current status and future prospects", Reports on Progress in Physics **81**, 066201 (2018).

[7]M. Schumann, "Direct detection of WIMP dark matter: concepts and status", Journal of Physics G: Nuclear and Particle Physics **46**, 103003 (2019).

[8]F. D. Steffen, "Dark-matter candidates: Axions, neutralinos, gravitinos, and axinos", en, The European Physical Journal C **59**, 557–588 (2009).

[9]S. P. Liew et al., "Mono-X versus direct searches: simplified models for dark matter at the LHC", en, Journal of High Energy Physics **2017**, 82 (2017).

[10]M. Ackermann et al., "Searching for Dark Matter Annihilation from Milky Way Dwarf Spheroidal Galaxies with Six Years of Fermi Large Area Telescope Data", en, Physical Review Letters **115**, 231301 (2015).

[11]L. Rinchiuso, "Latest results on dark matter searches with H.E.S.S", EPJ Web of Conferences **209**, edited by M. De Vincenzi, A. Capone, and A. Morselli, 01023 (2019).

[12]M. Aartsen et al., "Improved limits on dark matter annihilation in the Sun with the 79-string IceCube detector and implications for supersymmetry", Journal of Cosmology and Astroparticle Physics **2016**, 022–022 (2016).

[13]S. Adrián-Martínez et al., "Limits on dark matter annihilation in the sun using the ANTARES neutrino telescope", en, Physics Letters B **759**, 69–74 (2016).

[14]O. Adriani et al., "Cosmic-Ray Positron Energy Spectrum Measured by PAMELA", en, Physical Review Letters **111**, 081102 (2013).

[15]AMS Collaboration et al., "Properties of Cosmic-Ray Sulfur and Determination of the Composition of Primary Cosmic-Ray Carbon, Neon, Magnesium, and Sulfur: Ten-Year Results from the Alpha Magnetic Spectrometer", Physical Review Letters **130**, 211002 (2023).

[16]XENON Collaboration et al., "First Dark Matter Search with Nuclear Recoils from the XENONnT Experiment", Physical Review Letters **131**, 041003 (2023).

[17]A. M. Suliga, "Diffuse supernova neutrino background", `10.48550/ARXIV.2207.09632` (2022).

[18]G. Aad et al., "Observation of a new particle in the search for the Standard Model Higgs boson with the ATLAS detector at the LHC", en, Physics Letters B **716**, 1–29 (2012).

[19]*The Standard Model of Particle Physics — symmetry magazine*, `https://www.symmetrymagazine.org/standard-model/` (visited on 06/21/2023).

[20]M. Aker et al., "Direct neutrino-mass measurement with sub-electronvolt sensitivity", en, Nature Physics **18**, 160–166 (2022).

[21]X.-J. Xu, Z. Wang, and S. Chen, "Solar neutrino physics", en, Progress in Particle and Nuclear Physics **131**, 104043 (2023).

[22]Y. Suzuki, "The Super-Kamiokande experiment", en, The European Physical Journal C **79**, 298 (2019).

[23]A. Bellerive et al., "The Sudbury Neutrino Observatory", en, Nuclear Physics B **908**, 30–51 (2016).

[24]D. Z. Freedman, "Coherent effects of a weak neutral current", en, Physical Review D **9**, 1389–1392 (1974).

[25]D. Akimov et al., "Observation of coherent elastic neutrino-nucleus scattering", en, Science **357**, 1123–1126 (2017).

[26]R. Strauss et al., "The ν-cleus experiment: a gram-scale fiducial-volume cryogenic detector for the first detection of coherent neutrino–nucleus scattering", en, The European Physical Journal C **77**, 506 (2017).

[27]J. Billard, E. Figueroa-Feliciano, and L. Strigari, "Implication of neutrino backgrounds on the reach of next generation dark matter direct detection experiments", en, Physical Review D **89**, 023524 (2014).

[28]A. Bernstein et al., "*Colloquium* : Neutrino detectors as tools for nuclear security", en, Reviews of Modern Physics **92**, 011003 (2020).

[29]D. B. Collaboration, "A Precision Measurement of the Neutrino Mixing Angle theta_13 using Reactor Antineutrinos at Daya Bay", `10.48550/ARXIV.HEP-EX/0701029` (2007).

[30]The Double Chooz Collaboration, "Double Chooz θ13 measurement via total neutron capture detection", en, Nature Physics **16**, 558–564 (2020).

[31]H. Bonet et al., "Constraints on elastic neutrino nucleus scattering in the fully coherent regime from the CONUS experiment", Physical Review Letters **126**, 041804 (2021).

[32]M. Collaboration et al., *Background Studies for the MINER Coherent Neutrino Scattering Reactor Experiment*, 2016, `http://arxiv.org/abs/1609.02066` (visited on 08/13/2023).

[33]J. Billard et al., "Coherent Neutrino Scattering with Low Temperature Bolometers at Chooz Reactor Complex", Journal of Physics G: Nuclear and Particle Physics **44**, 105101 (2017).

[34]J. Rothe et al., "NUCLEUS: Exploring Coherent Neutrino-Nucleus Scattering with Cryogenic Detectors", en, Journal of Low Temperature Physics **199**, 433–440 (2020).

[35]D. Y. Akimov et al., "First ground-level laboratory test of the two-phase xenon emission detector RED-100", Journal of Instrumentation **15**, `10.1088/1748-0221/15/02/P02020` (2020).

[36]B. K. Cogswell, A. Goel, and P. Huber, "Passive Low-Energy Nuclear-Recoil Detection with Color Centers", en, Physical Review Applied **16**, 064060 (2021).

[37]K. Alfonso et al., "Passive low energy nuclear recoil detection with color centers – PALEOCCENE", 10.48550/arXiv.2203.05525 (2022).

[38]A. Aguilar-Arevalo et al., "Constraints on Light Dark Matter Particles Interacting with Electrons from DAMIC at SNOLAB", Physical Review Letters **123**, 181802 (2019).

[39]S. Collaboration et al., "Constraints on low-mass, relic dark matter candidates from a surface-operated SuperCDMS single-charge sensitive detector", Physical Review D **102**, 091101 (2020).

[40]R. J. D. Tilley, *Colour and the Optical Properties of Materials: An Exploration of the Relationship Between Light, the Optical Properties of Materials and Colour*, en, 1st ed. (Wiley, 2010).

[41]C. Kittel, *Introduction to solid state physics*, 8th ed (Wiley, Hoboken, NJ, 2005).

[42]P. A. Santi, "Light Sheet Fluorescence Microscopy: A Review", en, Journal of Histochemistry & Cytochemistry **59**, 129–138 (2011).

[43]J. Morris et al., "Molecular dynamics investigation of threshold displacement energies in CaF2", en, Computational Materials Science **172**, 109293 (2020).

[44]P. J. Worsfold, A. Townshend, and C. F. Poole, *Encyclopedia of analytical science*, eng (Elsevier, S.l., 2010).

[45]F. F. Voigt et al., "The mesoSPIM initiative: open-source light-sheet microscopes for imaging cleared tissue", en, Nature Methods **16**, 1105–1108 (2019).

[46]N. Vladimirov et al., *The Benchtop mesoSPIM: a next-generation open-source light-sheet microscope for large cleared samples*, en, preprint (Neuroscience, 2023).

[47]*Lightsheet - MesoSPIM (Irchel)*, en, http://www.zmb.uzh.ch/en/Available-Systems/LightMicroscopes/LightSheetMicroscopy/Light-sheet-MesoSPIM-(Irchel).html (visited on 08/10/2023).

[48]G. R. Araujo, "Phd thesis (under preparation), university of zurich", (2023).

[49]*Sklearn.cluster.DBSCAN*, en, https://scikit-learn/stable/modules/generated/sklearn.cluster.DBSCAN.html (visited on 08/13/2023).

[50] *Sklearn.cluster.KMeans*, en, https://scikit-learn/stable/modules/generated/sklearn.cluster.KMeans.html (visited on 08/13/2023).

[51] *Image filtering — Image analysis in Python*, https://scikit-image.org/skimage-tutorials/lectures/1_image_filters.html (visited on 08/13/2023).

[52] *Template Matching — skimage 0.21.0 documentation*, https://scikit-image.org/docs/stable/auto_examples/features_detection/plot_template.html (visited on 08/14/2023).

[53] P. Huber, "Private communication with patrick huber",

[54] *James Ziegler - SRIM & TRIM*, http://www.srim.org/ (visited on 08/15/2023).

[55] L. C. Courrol et al., "Color center production by femtosecond pulse laser irradiation in LiF crystals", EN, Optics Express **12**, 288–293 (2004).

[56] B. D. Evans, G. J. Pogatshnik, and Y. Chen, "Optical properties of lattice defects in α-Al2O3", Nuclear Instruments and Methods in Physics Research Section B: Beam Interactions with Materials and Atoms **91**, 258–262 (1994).

[57] A. Wald and J. Wolfowitz, "On a Test Whether Two Samples are from the Same Population", en, The Annals of Mathematical Statistics **11**, 147–162 (1940).

[58] V. Aerne, *Spreadsheet containing microscopy data information*, https://docs.google.com/spreadsheets/u/1/d/1wIwPkauWMJXGanfccUJnwgTPBkG1N3J7UAl_hxCLa0c/edit#gid=0 (visited on 08/24/2023).

[59] L. J. P., "Fast normalized cross-correlation", Vision Interface, 1995 **95**, 120 (1995).